

Lensing by Binary Galaxies Modelled as Isothermal Spheres

E.M. Shin* and N.W. Evans*

Institute of Astronomy, University of Cambridge, Madingley Road, Cambridge, CB3 0HA, United Kingdom

25 October 2018

ABSTRACT

We consider the problem of lensing by binary galaxies idealized as two isothermal spheres. This is a natural extension of the problem of lensing by binary point masses first studied by Schneider & Weiss (1986). In a wide binary, each galaxy possesses individual tangential, nearly astroidal, caustics and roundish radial caustics. As the separation of the binary is made smaller, the caustics undergo a sequence of metamorphoses. The first metamorphosis occurs when the tangential caustics merge to form a single six-cusped caustic, lying interior to the radial caustics. At still smaller separations, the six-cusped caustic undergoes the second metamorphosis and splits into a four-cusped caustic and two three-cusped caustics, which shrink to zero size (an elliptic umbilic catastrophe) before they enlarge again and move away from the origin perpendicular to the binary axis. Finally, a third metamorphosis occurs as the three-cusp caustics join the radial caustics, leaving an inner distorted astroid caustic enclosed by two outer caustics. The maximum number of images possible is 7. Classifying the multiple imaging according to critical isochrones, there are only 8 possibilities: 2 three-image cases, 3 five-image cases, and 3 seven-image cases. When the isothermal spheres are singular, the core images vanish into the central singularity. The number of images may then be 1, 2, 3, 4 or 5, depending on the source location, and the separation and masses of the pair of lensing galaxies. The locations of metamorphoses, and the onset of threefold and fivefold multiple imaging, can be worked out analytically in this case.

Key words: gravitational lensing – dark matter

1 INTRODUCTION

The Cambridge Sloan Survey of Wide Arcs in the Sky (CASSOWARY, see Belokurov et al. 2007, 2008) has uncovered a number of examples of gravitational lensing by luminous red galaxies (LRGs). For example, the lens CASSOWARY 2 has two very bright and massive LRGs at redshifts of $z = 0.426$ and 0.432 respectively acting as lenses for a blue star-forming galaxy at $z = 0.970$. Although the LRGs lie in a loose group, a natural starting point is that the lens is a close pair of galaxies. CASSOWARY 5 has two early-type galaxies separated by $\sim 5''$ on the sky acting as lenses. The three images of the high redshift source visible in the Sloan Digital Sky Survey data straddle the two lenses. CASSOWARY's search strategy has proved adept at finding gravitational lenses with large separation images ($\gtrsim 3''$), which naturally enough are typically caused by two or lensing galaxies. There are also a number of existing strong lenses for which there appears to be more than one lensing galaxy – such as HE 0230-213 (Wisotzki et al. 1999), PMN J0134-0931 (Winn et al. 2003) and B1359+154 (Rusin et al. 2001). In fact, in roughly a quarter of all strong lenses, the lensing potential is known to be more complex than a single lensing galaxy, with usually a pair or group of galaxies being implicated.

The only binary lens that has so far received detailed scrutiny

is the important case of two point masses. Schneider & Weiss (1986) carried out a detailed study of the caustics, critical curves and imaging properties. In particular, they showed that the simpler model of a point mass plus external shear (Chang & Refsdal 1984; An & Evans 2006) is not always a reliable description of the lensing properties of binary point masses. Given the importance of microlensing surveys for planets, there has been much subsequent theoretical work on the binary point mass case (see e.g., Witt 1990; Mao & Paczynski 1991; Witt & Mao 1995; Asada 2002). The theory has borne fruit in detailed modelling of binary lens events, including the first microlens mass determinations (An et al. 2002), and the discovery of the first Neptune mass extra-solar planets (Beaulieu et al. 2006).

Here, we provide a theoretical treatment of the problem of lensing by two isothermal spheres. The model has been considered numerically in Kochanek & Apostolakis (1988), though primarily in the context of lensing in two planes at different redshifts. The motivation of our study is threefold. First, a binary galaxy model has a direct application to the close galaxy pair lenses found by the CASSOWARY survey or to groups and clusters acting as lenses. Second, the investigation of the properties of highly non-symmetric gravitational lenses is seriously incomplete, and so the model provides an interesting counterweight to the binary point mass case. Third, in the case of binary singular isothermal spheres, many of the properties can be found analytically, giving insights that are not

* E-mail: ems@ast.cam.ac.uk; nwe@ast.cam.ac.uk

so easy to obtain using numerical work. The number of lenses for which analytic progress can be made is still very small.

The paper is organised as follows. In Section 2, we numerically examine the different possible critical curve topologies of two cored isothermal spheres. Different image configurations are explored by considering the Fermat surfaces in Section 3, and Section 4 deals with the special case of singular isothermal spheres, and derives a number of exact results.

2 TWO CORED ISOTHERMAL SPHERES

2.1 Models

We use dimensionless source plane $\xi = (\xi, \eta)$ and lens plane coordinates $\mathbf{x} = (x, y)$ (see e.g., Schneider et al. 1992). The two isothermal spheres are centred at $\pm a$ on the x -axis. The deflection potential is

$$\psi(x, y) = E_1 [r_{c_1}^2 + (x+a)^2 + y^2]^{1/2} + E_2 [r_{c_2}^2 + (x-a)^2 + y^2]^{1/2}, \quad (1)$$

where r_{c_1} and r_{c_2} are the core radii of the isothermal spheres. If the core radii vanish, this reduces to the potential of two singular isothermal spheres with Einstein radii E_1 and E_2 . We take $E_1 \leq E_2$ and $a > 0$ without loss of generality.

Let us introduce $r_1^2 = (a+x)^2 + y^2$ and $r_2^2 = (a-x)^2 + y^2$. Then the convergence is

$$\kappa(\mathbf{x}) = \frac{E_1}{2} \frac{2r_{c_1}^2 + r_1^2}{(r_{c_1}^2 + r_1^2)^{3/2}} + \frac{E_2}{2} \frac{2r_{c_2}^2 + r_2^2}{(r_{c_2}^2 + r_2^2)^{3/2}}. \quad (2)$$

whilst the shear components are

$$\gamma_1(\mathbf{x}) = \frac{E_1 y^2 - (a+x)^2}{2 (r_{c_1}^2 + r_1^2)^{3/2}} + \frac{E_2 y^2 - (a-x)^2}{2 (r_{c_2}^2 + r_2^2)^{3/2}}, \quad (3a)$$

$$\gamma_2(\mathbf{x}) = E_2 \frac{(a-x)y}{(r_{c_2}^2 + r_2^2)^{3/2}} - E_1 \frac{(a+x)y}{(r_{c_1}^2 + r_1^2)^{3/2}}. \quad (3b)$$

The Jacobian of the lens mapping may be found either from

$$\det \mathbf{A}(\mathbf{x}) = [1 - \psi_{xx}(\mathbf{x})][1 - \psi_{yy}(\mathbf{x})] - \psi_{xy}(\mathbf{x})^2, \quad (4)$$

or from

$$\det \mathbf{A}(\mathbf{x}) = [1 - \kappa(\mathbf{x})]^2 - \gamma(\mathbf{x})^2, \quad (5)$$

where the magnitude of shear is

$$\gamma(\mathbf{x}) = \sqrt{\gamma_1(\mathbf{x})^2 + \gamma_2(\mathbf{x})^2}. \quad (6)$$

For an isolated, singular isothermal sphere, $\gamma = \kappa$ and so we obtain the familiar result $\det \mathbf{A} = 1 - 2\kappa$. The analogue of this in the binary, singular case is

$$\det \mathbf{A} = 1 - 2\kappa + 4E_1 E_2 \frac{a^2 y^2}{r_1^3 r_2^3} \quad (7)$$

and so $\det \mathbf{A} = 1 - 2\kappa$ on the axis of two singular isothermal spheres.

2.2 Two Identical Galaxies with Varying Separation

Let us take as properties of a fiducial elliptical galaxy lens a velocity dispersion $\sigma = 250 \text{ km s}^{-1}$, a core radius $r_{c_1} = r_{c_2} = 100 \text{ pc}$, and a redshift $z_1 = 0.46$. Let us take the source redshift as $z_s = 2.15$, and use a Λ CDM concordance cosmology. As shown

in Shin & Evans (2008), this choice of parameters is astrophysically reasonable. The corresponding dimensionless Einstein radius is $E \approx 7.11$ (where the length scale is chosen to be 1 kpc). We place two such fiducial isothermal spheres at $(-a, 0)$ and $(+a, 0)$, and numerically find critical curves and caustics for varying a . The different possible configurations are shown in Fig. 1.

When a is large (top-most panels of Fig. 1), the critical curves and caustics of the two lenses are disjoint, but the outer tangential critical curves are not circular (as they would be for a single such lens in isolation) and the corresponding caustics are distorted astroids with four cusps. There are small radial critical curves around each lens that map to large roundish caustics. We call this configuration of critical curves, and the corresponding caustic configuration, ‘Type 0’. For $a = 10.0$, the tangential critical curves have merged into a single outer critical curve (which we call the common tangential critical curve), and the corresponding caustics have merged to form a single six-cusp caustic. We call this arrangement ‘Type 1’. The six-cusp caustic elongates along the y -axis as a decreases further, and two small three-cusp caustics split off, as two small critical curves (henceforth ‘bean’ critical curves) pinch off from the outermost critical curve, to leave a single four-cusp astroid caustic ($a = 5.6$ and $a = 5.4$). We call this ‘Type 2’. The physical origin of the ‘bean’ critical curves is explained later (§ 4.4) in the context of singular isothermal spheres. At $a = 4.0$, the three-cusp caustics have moved away from the origin and enlarged, whilst the ‘bean’ critical curves have moved towards the origin and enlarged. Decreasing a still further, the two ‘bean’ critical curves merge with the two radial critical curves, creating two critical curves around the origin (bottom-most panels). The inner one maps to a caustic with two butterfly cusps, whilst the outer one maps to the outermost caustic. The outermost critical curve still corresponds to an astroid caustic around the origin. We call this configuration ‘Type 3b’.

2.3 Two Galaxies with Different Einstein Radii E_1 and E_2

Although there are five free parameters in (1), the geometry of the critical curves and caustics are determined by four. This is most easily seen from the lens equation

$$\xi = x - E_1 \frac{(x+a)}{(r_{c_1}^2 + r_1^2)^{1/2}} - E_2 \frac{(x-a)}{(r_{c_2}^2 + r_2^2)^{1/2}} \quad (8a)$$

$$\eta = y \left[1 - \frac{E_1}{(r_{c_1}^2 + r_1^2)^{1/2}} - \frac{E_2}{(r_{c_2}^2 + r_2^2)^{1/2}} \right]. \quad (8b)$$

If all five parameters are scaled by λ , the new lens has the same critical curve and caustic geometry, just on a different scale: choosing new coordinates $(x', y') = \lambda^{-1}(x, y)$, $(\xi', \eta') = \lambda^{-1}(\xi, \eta)$ reduces the new lens equation to the old one.

Now, the most physically interesting regime has $r_c \ll a$ – that is, the separation between the two lensing galaxies is much larger than their core radii – whilst E_1, E_2 and a are comparable. The scaling degeneracy means that it is only the ratios E_1/a and E_2/a that determine the geometry of the critical curves and caustics (up to the effect of the core radii). So we fix a (to 10, specifically), allow E_1 and E_2 to vary, and find which critical curve geometries arise from different parts of the E_1 - E_2 parameter plane. Since only small core radii are physical, we do not explore the r_{c_1} and r_{c_2} dimensions of parameter space much. For simplicity, r_{c_1, c_2} are set to scale with $E_{1,2}$ as $(0.1/7.11)E_{1,2}$ respectively, so that a doubling of both E_i corresponds, physically, to halving the separation $2a$ be-

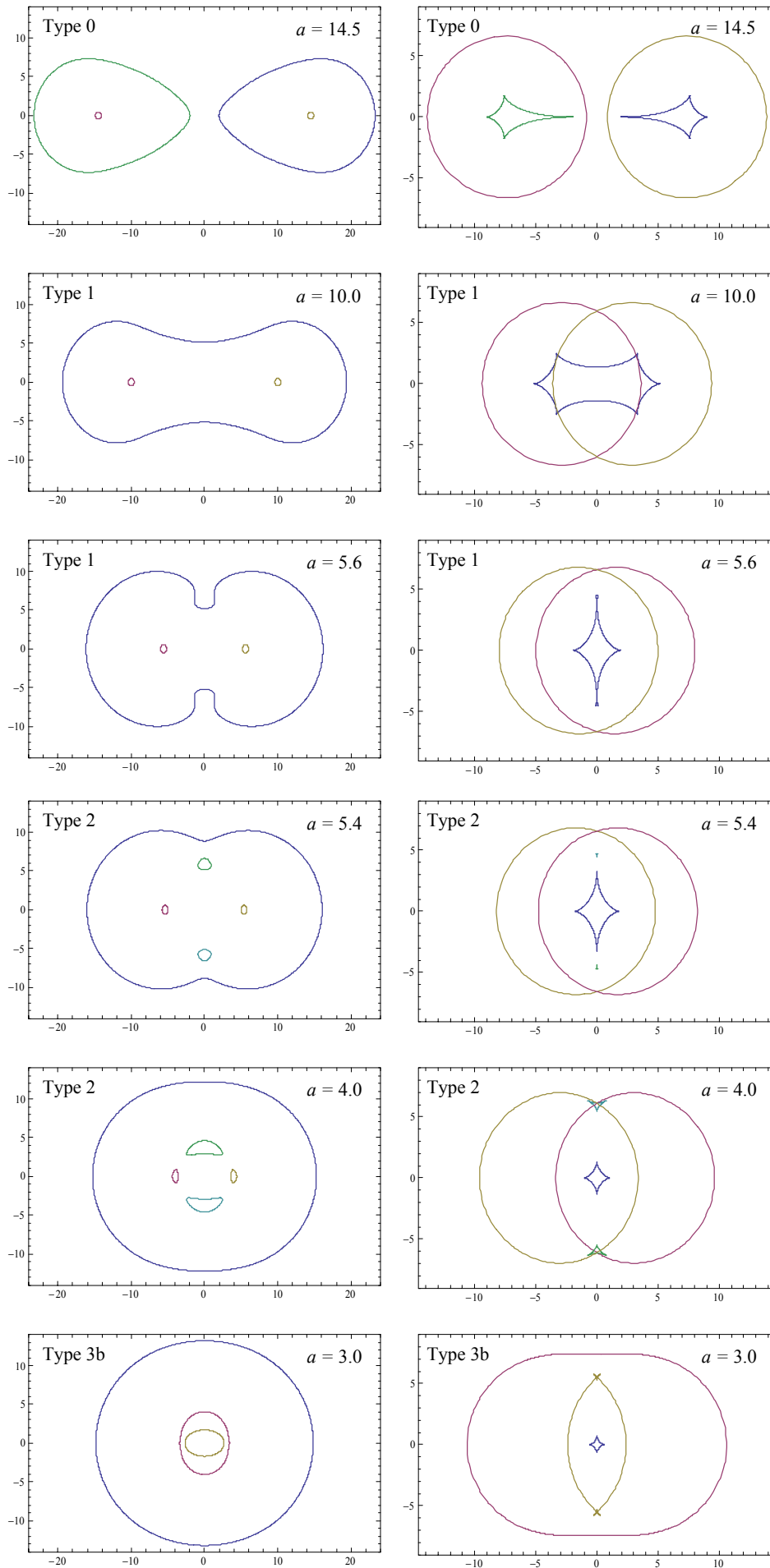


Figure 1. Critical curves (left panels) and caustics (right panels) for two identical fiducial isothermal spheres (with dimensionless Einstein radius ~ 7.11) separated by dimensionless distance $2a$. Colours of corresponding critical curves and caustics match. The *Type* of the critical-curves or caustics is defined in the text.

tween the lens galaxies. (The factor $(0.1/7.11)$ normalizes the core radii to the fiducial isothermal spheres.)

We find that there are five possible critical curve topologies. There are the four seen in § 2.2: Type 0 (disjoint tangential critical curves), Type 1 (a common tangential critical curve), Type 2 (a common tangential critical curve surrounding two ‘bean’ critical curves in addition to the two radial critical curves), and Type 3b (the common tangential critical curve, and two other critical curves in a distorted annulus around the origin, with the galaxy centres lying within the edges of the annulus). In addition, there is a Type 3a topology: unequal isothermal spheres mean that the two ‘bean’ critical curves merge with one of the radial critical curves before the other. These five critical curve topologies are separated by four metamorphoses of critical curve geometry, as shown in Figures 2 to 5, which we call Metamorphoses 1, 2, 3a and 3b. Metamorphosis 1 marks the transition from Type 0 to Type 1 critical curves, and so on. Recall when viewing these figures that E_i are always dimensionless Einstein radii (in the same units as the axes) and that the isothermal spheres are centred at ± 10 on the x -axis.

The metamorphoses of caustics occur at metamorphoses of the critical curves, except for the development of swallowtails in one of the caustics without any corresponding change in the topology of the critical curves: see Fig. 6. (For the mathematical background to catastrophe theory, see e.g., Arnold 1986, whilst for an introduction to critical-curve and caustic metamorphoses, see e.g. Petters et al. 2001.) So we also call caustics Type 0, 1 and so on if the critical curves are of that type. Note, however, an astroid caustic can still pierce a radial caustic, for example, without the critical curve topology changing. But caustics do not merge or split unless the critical curves do.

In Type 0 critical curves, $\det \mathbf{A} > 0$ outside the tangential critical curves, and $\det \mathbf{A} < 0$ within them except for the small regions within the radial critical curves around the galaxy centres at $(\pm a, 0)$. There is a saddle of $\det \mathbf{A}$ on the x -axis, and as E_i are increased, $\det \mathbf{A}$ at the saddle decreases. As the saddle decreases through zero, the two regions of negative $\det \mathbf{A}$ link up, forming Type 1 critical curves (Metamorphosis 1, Fig 2). The corresponding metamorphosis in the caustics is the merging of the two four-cusp astroids, via a ‘beak-to-beak’ transition (see e.g., Schneider et al. 1992, Chap. 6), into a six-cusped curve, which we henceforth call a ‘hexacuspoid’. Note also that the hexacuspoid can pierce the radial caustics.

As E_i are increased further, the outer, common tangential critical curve loses its bottleneck, but eventually develops dimples around two small regions that have more positive $\det \mathbf{A}$ than their surroundings (these are regions where the shear is small: see § 4.4). Meanwhile, the hexacuspoid becomes less elongated along the x -axis and more elongated in the y -axis. Increase E_i still more and Metamorphosis 2 occurs (Fig. 3): the dimple in the tangential critical curve closes completely around the small regions of positive $\det \mathbf{A}$, creating two ‘bean’ critical curves. The two small three-cusp caustics split off from the tangential caustic via beak-to-beak metamorphoses.

At still larger E_i , the ‘bean’ critical curves extend towards the radial critical curves whilst the three-cusp caustics move outwards towards the radial caustics. When $E_2 \lesssim 20$, we have Metamorphosis 3a (Fig. 4: the beans merge with the left-hand radial critical curve, forming what we call the ‘Pacman’ critical curve ¹, and the

three-cusp caustics tack on to the corresponding radial caustic). As E_1 reaches $\lesssim 20$, the ‘Pacman’ critical curve merges with the remaining radial critical curve (Metamorphosis 3b, Fig. 5) to form an annular region of positive $\det \mathbf{A}$, as the caustics change accordingly (via hyperbolic umbilic metamorphoses again).

The five critical curve regimes (Types 0, 1, 2, 3a and 3b), into which the E_1 - E_2 parameter plane is divided by the four critical curve metamorphoses, are shown in Fig. 7. Recall that we have fixed $a = 10$ because the critical curve and caustic geometry is dependent mainly on the ratios $E_{1,2}/a$ and $r_{c1,2}/a$ in the astrophysically important regime of $a \gg r_{c1,2}$. For small core radii, there is a good analytic approximation (which is exact for singular isothermal spheres – see § 4.3) for the lens parameters E_1, E_2, a at which Metamorphosis 1 (the merging of the two tangential critical curves) occurs. The other metamorphoses are determined by numerically finding critical curves and caustics for various E_i . Metamorphoses 3a and 3b depend very strongly on $r_{c1,c2}$, whilst Metamorphoses 1 and 2 don’t, as might be expected.

Higher order catastrophes such as swallowtails have been noted before in a variety of lens models (Keeton et al. 2000; Evans & Witt 2001; Bradač et al. 2004). Swallowtails can form for Types 3a and 3b; regions in the E_1 - E_2 plane where the caustics have swallowtails are denoted by 3aS and 3bS. The lower-right of Fig. 7, which is left blank, is – by the symmetry of the lens – just the reflection of the upper-left part of the plot in the line $E_1 = E_2$ (shown dotted).

From Fig. 7, we confirm that Type 0, 1, and 2 curves correspond to progressively stronger isothermal sphere lenses. The size of the core radii affects the size of the radial critical curves and hence when the radial and ‘bean’ critical curves merge via Metamorphoses 3a and 3b. As expected, increasing the core radii mean that the mergers take place at smaller E_i , as the radial critical curves enlarge (reaching out towards the bean critical curves). The reason that smaller core radii enlarge the swallowtail region of parameter space is that $r_c = 0$ singular isothermal spheres always have three-cusp caustics (see § 4).

It is also worth noting that the ‘bean’ critical curves and the corresponding three-cusp caustics pass through an elliptic umbilic catastrophe in parameter space (where they shrink to zero size), in-between Metamorphoses 2 and 3a. The condition on E_1, E_2 and a for this can be found exactly for the case $r_{c1} = r_{c2} = 0$ (see § 4.4), and remains a good approximation for small r_c .

3 IMAGE GEOMETRIES

There can be 1, 3, 5 or 7 images; the corresponding regions in the source plane can be easily deduced in Figures 1 to 5. Only one image is produced if the source is outside all the caustics, and there are two extra images for each caustic within which the source lies. Central images are usually highly demagnified and would not be observable, so some 3-image systems would appear as doublets (e.g. 3A-1 in Fig. 10), some 5-image systems as quadruplets (e.g. 5B-1 in Fig. 11) or even triplets (e.g. 5A-1 in Fig. 11), and 7-image systems usually as quintuplets (e.g. 7A-1 in Fig. 12). The different image geometries may be classified according to the topography of the Fermat potential (see e.g., Schneider et al. 1992), which is

$$\phi_{\xi}(\mathbf{x}) = \frac{1}{2}(\mathbf{x} - \xi)^2 - \psi(\mathbf{x}) \quad (9)$$

where $\xi = (\xi, \eta)$ and $\mathbf{x} = (x, y)$. A helpful visualization of eqn. (9) is provided by the Fermat time delay surface, examples

¹ Named after the characteristic shape of the protagonist in the eponymous computer game.

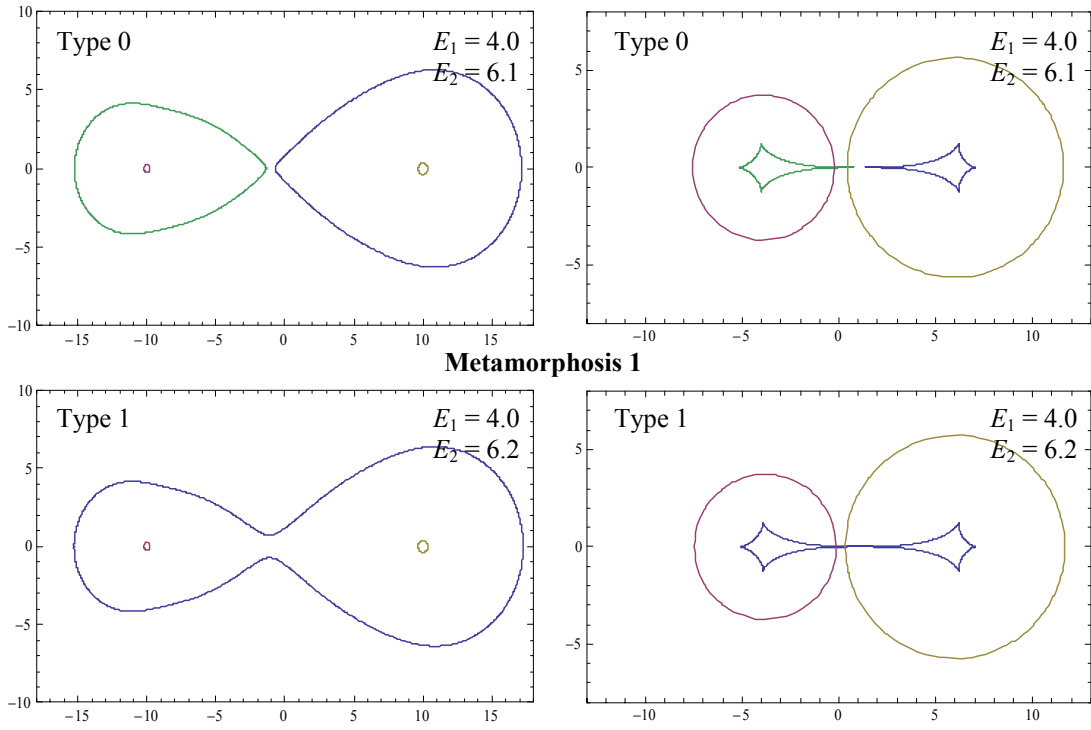


Figure 2. Critical curves (left panels) and caustics (right panels) of Metamorphosis 1, which takes us from Type 0 (upper panels) to Type 1 (lower panels) morphologies. E_1 and E_2 in the lower panels are greater than or equal to E_1 and E_2 in the upper panels. As in the case of identical isothermal spheres (Fig. 1), the two tangential critical curves merge, as do the corresponding distorted four-cusp astroid caustics.

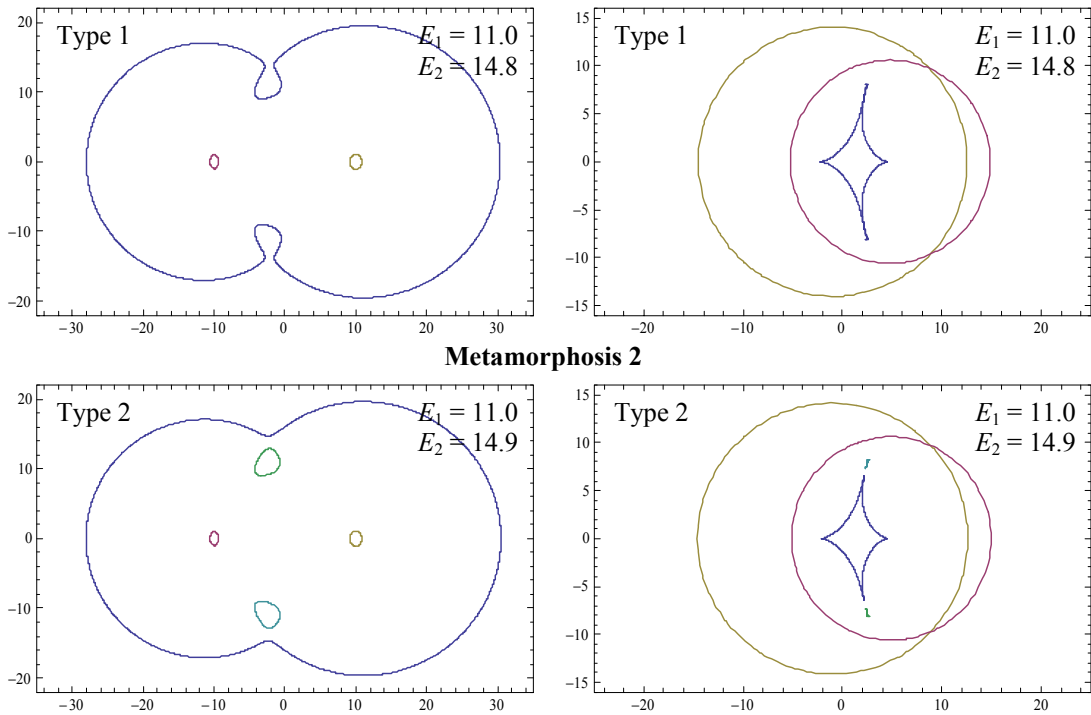


Figure 3. Critical curves (left panels) and caustics (right panels) of Metamorphosis 2, which takes us from Type 1 (upper panels) to Type 2 (lower panels) morphologies. E_1 and E_2 in the lower panels are greater than or equal to E_1 and E_2 in the upper panels. Two critical curves pinch off from the outer critical curve, corresponding to two three-cusp caustics pinching off from the hexacuspid caustic.

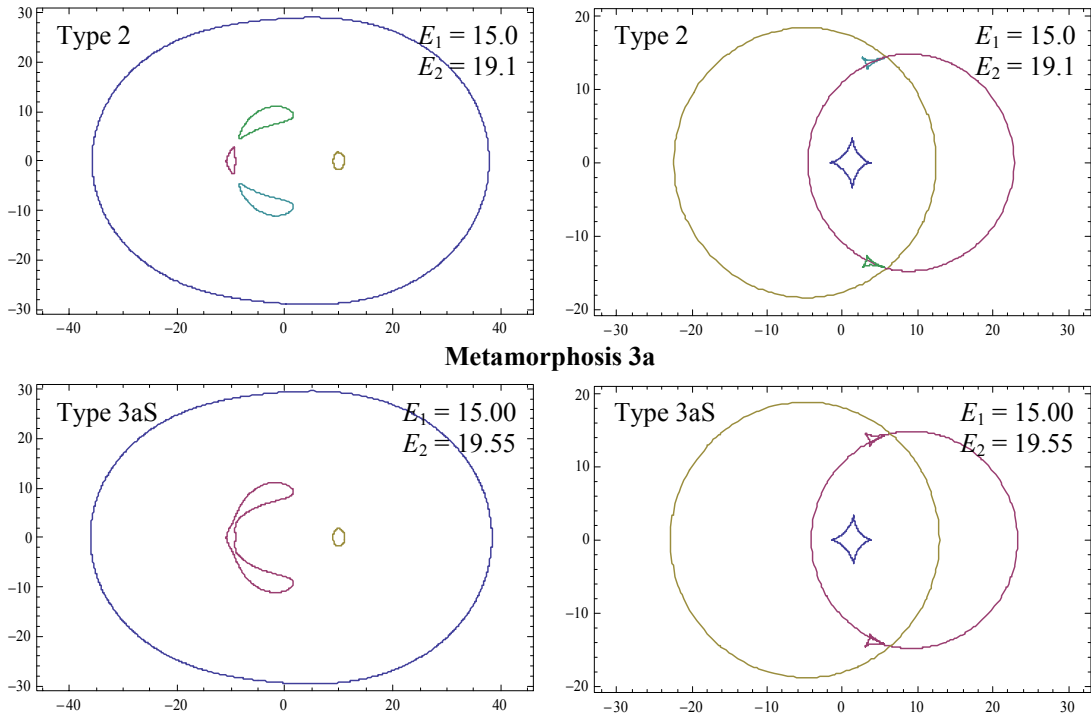


Figure 4. Critical curves (left panels) and caustics (right panels) of Metamorphosis ‘3a’. E_1 and E_2 in the lower panels are greater than or equal to E_1 and E_2 in the upper panels. (Metamorphoses 3a and 3b are distinct if $E_1 \neq E_2$.) In 3a, the two critical curves corresponding to the three-cusp caustics merge with one of the two small ‘radial’ critical curves to form a ‘Pacman’ critical curve. The three-cusp caustics merge with the corresponding radial caustic, giving it six cusps, although increasing E_2 further can reduce that to two cusps via a swallowtail folding (see Fig. 6).

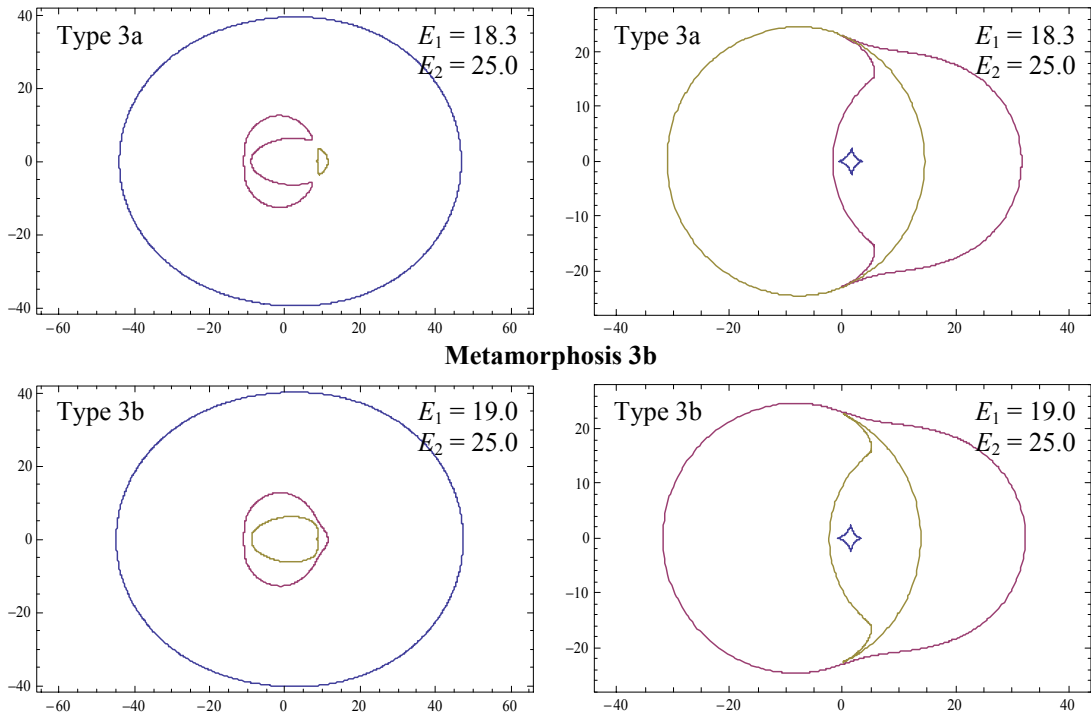


Figure 5. Critical curves (left panels) and caustics (right panels) of Metamorphosis ‘3b’. E_1 and E_2 in the lower panels are greater than or equal to E_1 and E_2 in the upper panels. The ‘Pacman’ critical curve merges with the remaining radial critical curve; the caustics change accordingly. (Swallowtails – see Fig. 6 – are not visible with the curves plotted on this scale.)

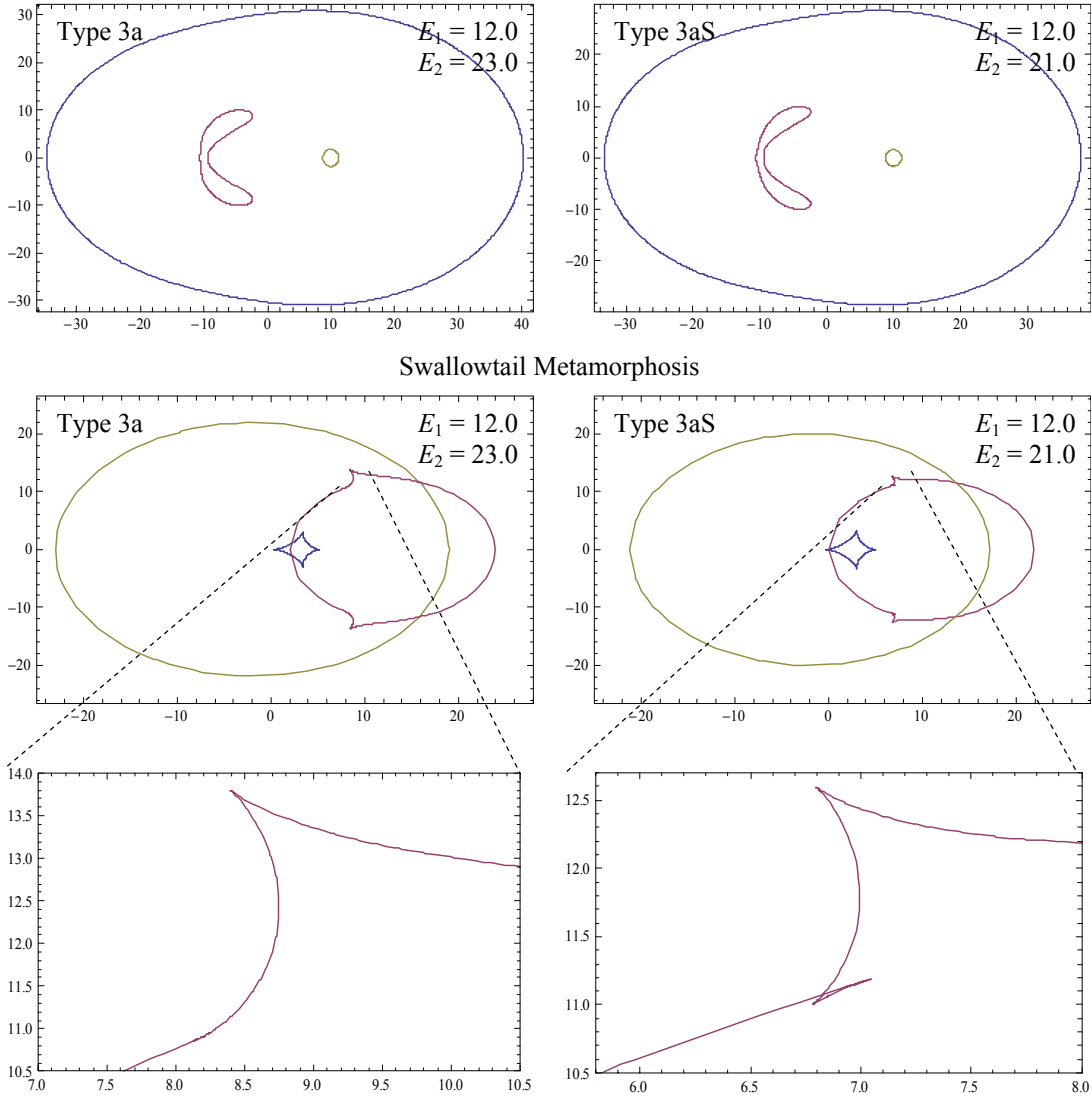


Figure 6. The Swallowtail Metamorphosis. Two of the three cusps in this caustic belong to a swallowtail unfolding. Note that critical curves are shown in the two *top* panels and caustics in the lower ones. E_1 and E_2 in the right panels are less than or equal to E_1 and E_2 in the left panels.

of which appear below (Figs 10 to 12). The images occur at stationary points of the Fermat surface $\nabla\phi = 0$, which may be local maxima, local minima, or saddles. (We exclude cases where y lies on a caustic, so there are no images at critical points.) Now, $\phi(\mathbf{x})$ looks like a concave-up paraboloid at large $|\mathbf{x}|$ because $\psi \rightarrow 0$ (or a constant), so level curves of $\phi(\mathbf{x})$ must be closed. Also, level curves cannot cross except at saddle points. A Fermat surface can therefore be classified by the topology of the level curves that run through saddles, the *critical isochrones*, (see e.g. Schneider et al. (1992) §5.5). There are four ways to close the critical isochrones that run through a saddle, as shown in Fig. 8, which we call Le^\pm (the lemniscates) and Li^\pm (the limaçons) for short. We recall that if there are 3, 5 or 7 images, there are 1, 2 or 3 saddle points, respectively. For a given number of saddle points, it is straightforward to count the number of possible critical isochrone topologies: it is a matter of counting the number of different ways in which limaçons and lemniscates can be enclosed within one another consistently, assuming that $\phi(S_i) \neq \phi(S_j)$ for different saddle points S_i, S_j (see e.g. Schneider et al. 1992). There are 2 possible topolo-

gies for 3-image geometries, 6 for 5-image geometries and 25 for 7-image geometries, but not all of these actually arise in a given lens model (Blandford & Narayan 1986).

Although there are many different possible topologies for the caustics (Types 0 to 3b, swallowtails, and different overlapping of caustics), that divide the source plane up into many different regions, there are only eight different critical isochrone topologies for the double isothermal sphere lens: two three-image cases, three five-image cases, and three seven-image cases. These are listed in Table 1, and the possible five- and seven-image topologies are shown explicitly in Fig. 9. We name them according to the shapes of the critical isochrones, starting from the outermost and working inwards; the exact placement of the limaçons and lemniscates follows implicitly. So, for example, $\text{Li}^+ \text{Li}^+ \text{Le}^-$ means that an outer limaçon encloses an inner limaçon (and an Li^+ can only be put inside the minus region of the outer limaçon), which in turn contains an innermost lemniscate (which must be in the minus region of the inner limaçon), whilst $\text{Li}^+ \text{Le}^+ \text{Le}^-$ means that there is a Le^+ in

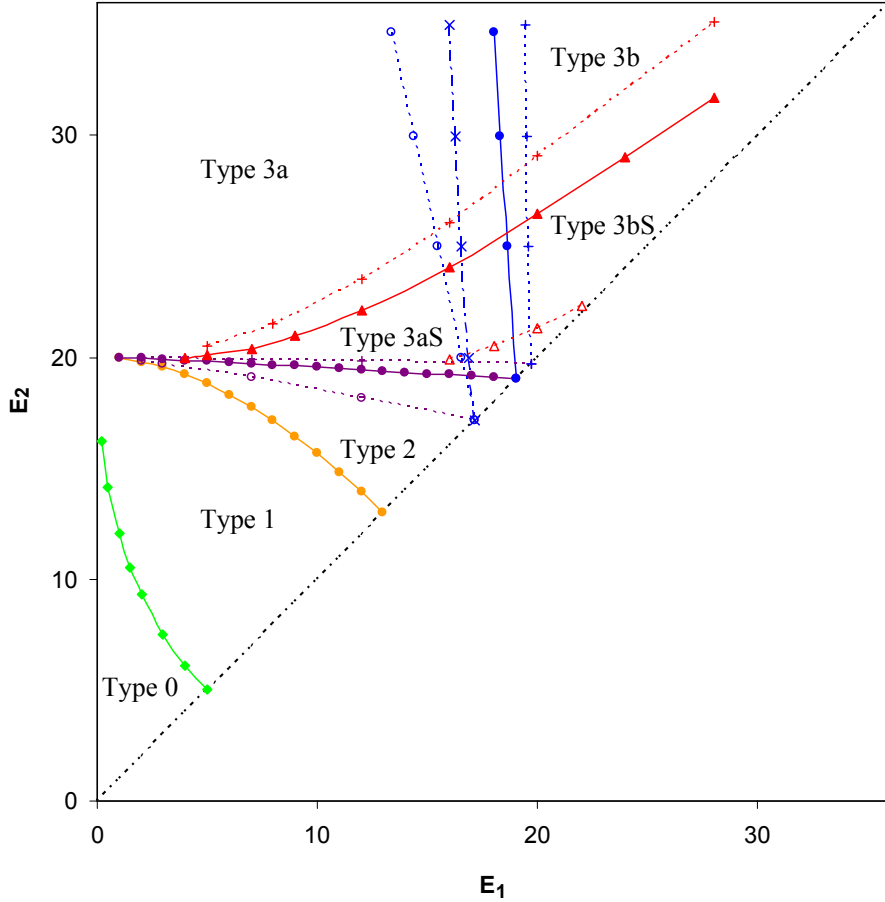


Figure 7. The critical curve metamorphoses divide E_1 - E_2 parameter space into regions of different critical curve and caustic geometries. Metamorphoses 1, 2, 3a and 3b are shown in green, orange, purple and blue, respectively. The swallowtail metamorphosis is shown in red. This plot is for $a = 10$, which is arbitrarily chosen: recall that the critical curves are determined (up to rescaling of axes) by the ratios E_1/a , E_2/a , r_{c1}/a and r_{c2}/a . Solid points and lines correspond to the fiducial scaling of the core radius $r_{c1,2} = (0.1/7.11)E_{1,2}$ (see §2.3), whilst open points are for $r_{c1,2}$ scaling as $5 \times (0.1/7.11)E_{1,2}$ and plus signs for $(1/5) \times (0.1/7.11)E_{1,2}$. The blue crosses are for Metamorphosis 3b (the metamorphosis most sensitive to core radii) with $r_{c1,2}$ fixed instead of scaling with E_i . Metamorphoses 1 and 2 are not significantly dependent on $r_{c1,2}$, whilst the other metamorphoses (especially 3b and the swallowtail) are very sensitive to them. Increasing $r_{c1,2}$ suppresses formation of swallowtail cusps and brings metamorphoses 3a and 3b to smaller $E_{1,2}$. The lines of metamorphoses 3a and 3b would approach $E_2 = 2a (= 20 \text{ here})$ and $E_1 = 2a (= 20)$ if $r_{c1} \rightarrow 0$, $r_{c2} \rightarrow 0$ (see § 4.5).

the plus region of the limaçon and a Le^- in the minus region (since a Le^- cannot be enclosed within a Le^+).

For the same isochrone topology, image configurations can differ qualitatively, as listed in the second column of the Table. So, for example, 7B-1 and 7B-2 are two distinct seven-image configurations corresponding to $\text{Li}^+ \text{Le}^+ \text{Le}^-$. Examples of qualitatively different image configurations are plotted in Figs 10 to 12, with image positions superimposed on critical curves and Fermat surfaces with critical isochrones. The galaxies are still always centred at $(\pm 10, 0)$ in these figures, and the core radii $r_{c1,2}$ are chosen as before.

Classifying image geometries by critical isochrone topology is of more than mathematical interest because it allows the order of arrival of images to be deduced (in whole or in part). But, as the figures show, systems with the same critical isochrone topology can be very different: they can have a different number of core images (as in examples 5C-1 and 5C-2 in Fig. 11), or the bright images may be positioned very differently (e.g. 7B-1 and 7B-2 in Fig. 12), and, since Fermat surfaces change smoothly with changing lens parameters and source position, two systems can have similar image positions but have different critical isochrone topologies. Indeed,

more than one critical isochrone topology is possible for sources in the same region of a given critical curve and caustic topology: for example, both the Fermat topographies $\text{Li}^+ \text{Li}^+ \text{Le}^-$ (e.g. 7A-1) and $\text{Li}^+ \text{Le}^+ \text{Le}^-$ (e.g. 7B) can arise from a Type-1 caustic configuration with the source inside all three caustics (not shown in Figures). It is also possible to obtain the same critical isochrone topology and similar image positions for lenses with topologically distinct critical curves and caustics (e.g. the two 7C-1 panels in Fig. 12).

4 TWO SINGULAR ISOTHERMAL SPHERES

When the isothermal spheres are singular ($r_{c1} = r_{c2} = 0$), the algebra is simpler than the cored ($r_{c1}, r_{c2} > 0$) case, and we derive some analytic results on critical curve and multiple-imaging regimes. Specifically, we find the pseudocaustics in § 4.1, which allows us (in § 4.2) to derive conditions on the lens parameters (E_1 , E_2 , a) for which three- and five-fold imaging becomes possible. We find the lens parameters for Metamorphosis 1 (in § 4.3),

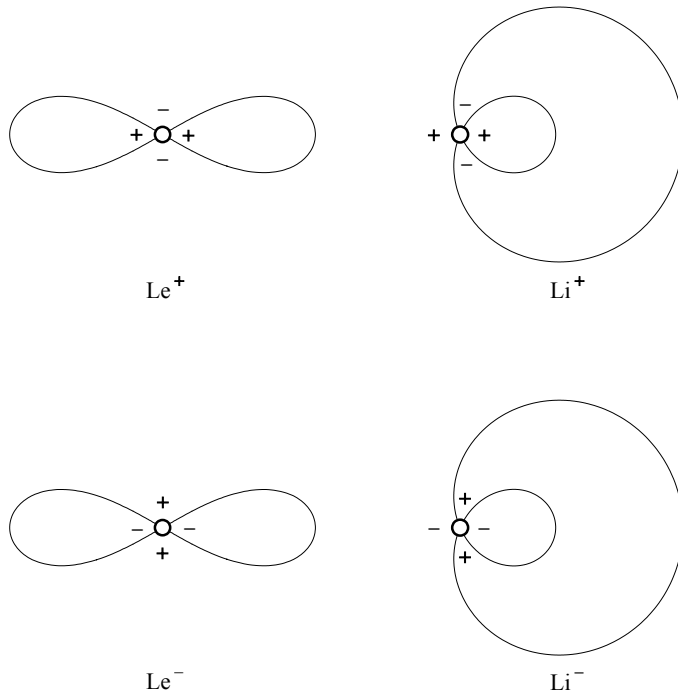


Figure 8. The four ways to close the critical isochrones of a single saddle point. The left panels show lemniscates, the right panels limaçons. Critical isochrone topologies for multiple saddles are constructed by combining these basic shapes.

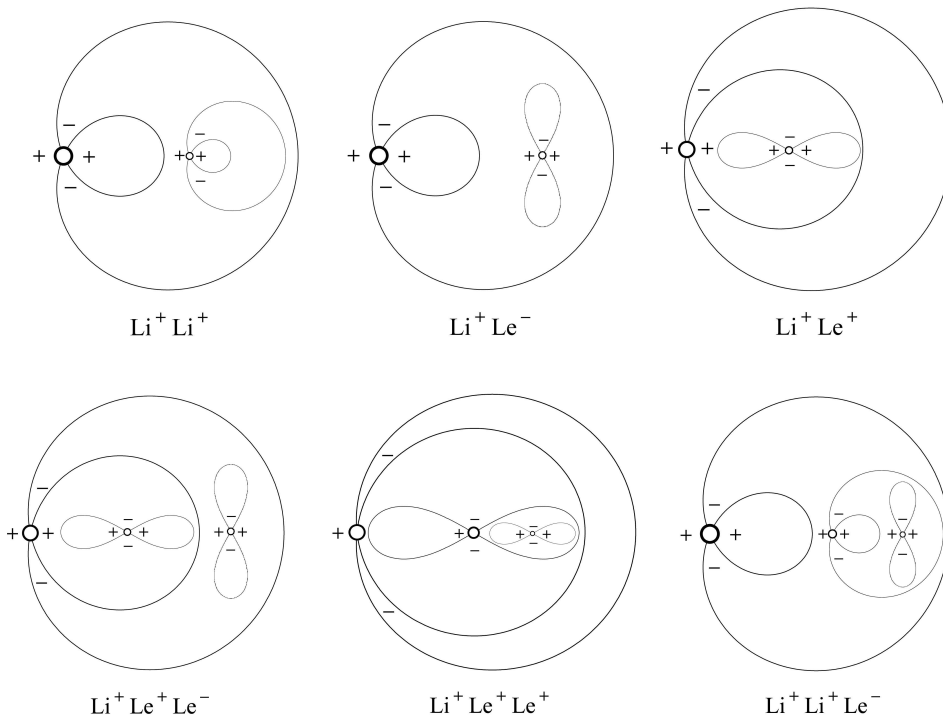


Figure 9. The five- and seven-image critical isochrone topologies that occur for the double isothermal sphere lens. They are named according to the shape of the critical isochrones (see Fig. 8), starting from the outermost.

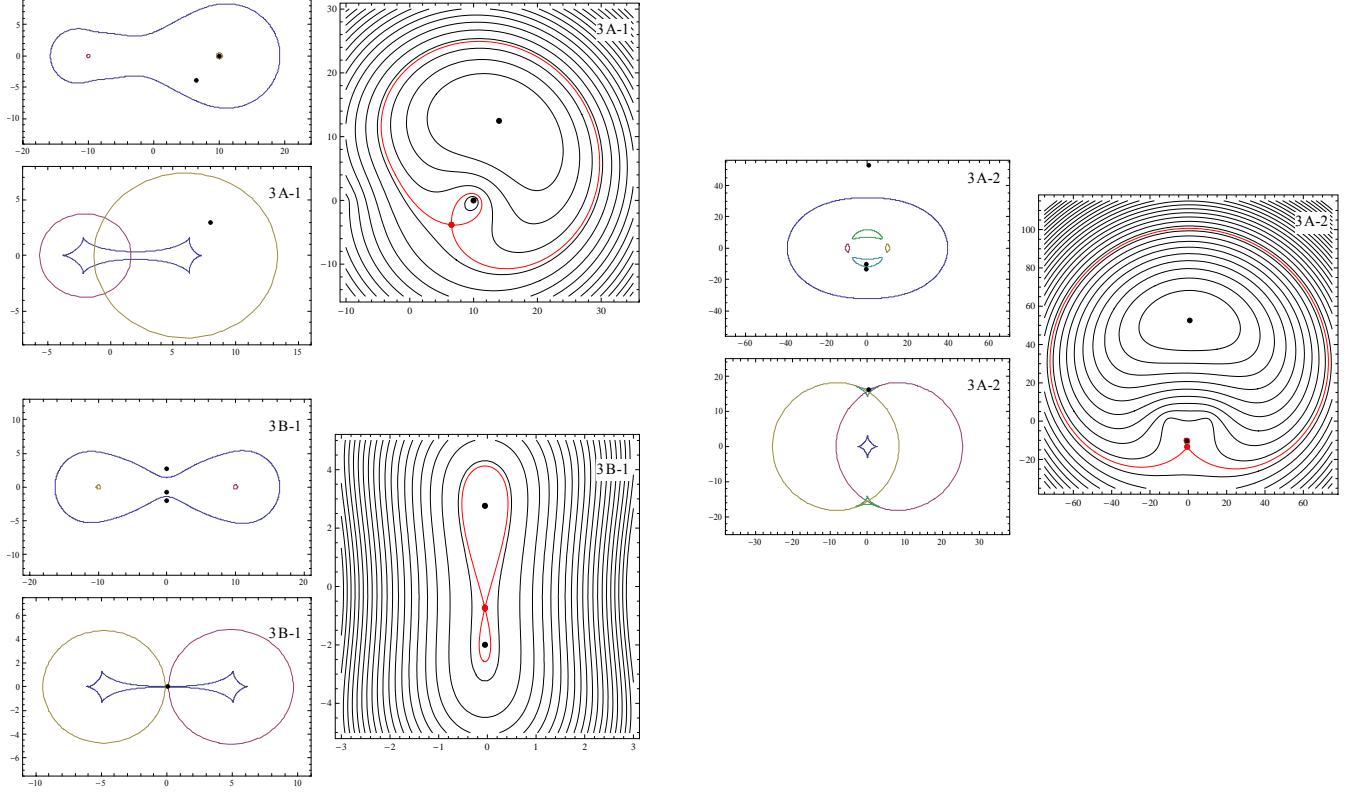


Figure 10. The different three-image Fermat surface topographies and image configurations. The left-hand panels show critical curves and image positions (upper panels of each example), and caustics and the position of the point source (lower panels). Colours of corresponding critical curves and caustics match. The right-hand panels show contours of the Fermat potential together with the saddle-points and their critical isochrones (red points and contours) as well as the images corresponding to the maximum and the minimum in the Fermat potential (black points). In example 3A-1, one of the three images is a highly-demagnified core image, whilst in 3B-1 all three images are of high magnification. The source in 3A-2 is inside a three-cusp caustic but outside both radial caustics. The critical isochrone is a limaçon, as in 3A-1, but this system would be observed as a triplet: the two images near the ‘bean’ critical curve are of high magnification, and the primary image is also magnified.

Table 1. The different Fermat surface topographies of a lens consisting of two non-singular isothermal spheres, and the critical curve configurations which can give rise to them.

Number of images	Critical isochrone topology	Name of example image configuration	Critical curve and caustic type	Source positions
Three images	Li^+	3A-1	Any type	Inside one radial (or ‘Pacman’) caustic only.
	Li^+	3A-2	Type 2	Inside a three-cusp caustic only
	Le^-	3B-1	Type 0, Type 1	Inside astroid or hexacuspoid caustic only.
Five images	$Li^+ Li^+$	5A-1	Type 1, 2	Inside both radial caustics only.
	$Li^+ Li^+$	5A-2	Type 2	Inside three-cusp caustic and one radial caustic only.
	$Li^+ Le^-$	5B-1	Any type	Inside astroid or hexacuspoid and one radial caustic only.
	$Li^+ Le^+$	5C-1	Type 3a(S), 3b(S)	Outside the astroid but inside both other caustics.
	$Li^+ Le^+$	5C-2	Type 3aS	Inside swallowtail but outside radial caustic.
Seven images	$Li^+ Li^+ Le^-$	7A-1	Type 1	Inside hexacuspoid and both radial caustics.
	$Li^+ Le^+ Le^-$	7B-1	Any type	Type 1: inside hexacuspoid and both radial caustics. Type 2: inside both radial caustics and the astroid or a three-cusp caustic. Types 3a(S), 3b(S): inside astroid and both other caustics.
	$Li^+ Le^+ Le^-$	7B-2	Type 2	Inside both radial caustics and a three-cusp caustic.
	$Li^+ Le^+ Le^+$	7C-1	Type 2	Inside both radial caustics and a three-cusp caustic.
			Types 3aS, 3bS	Inside swallowtail and the radial caustic.

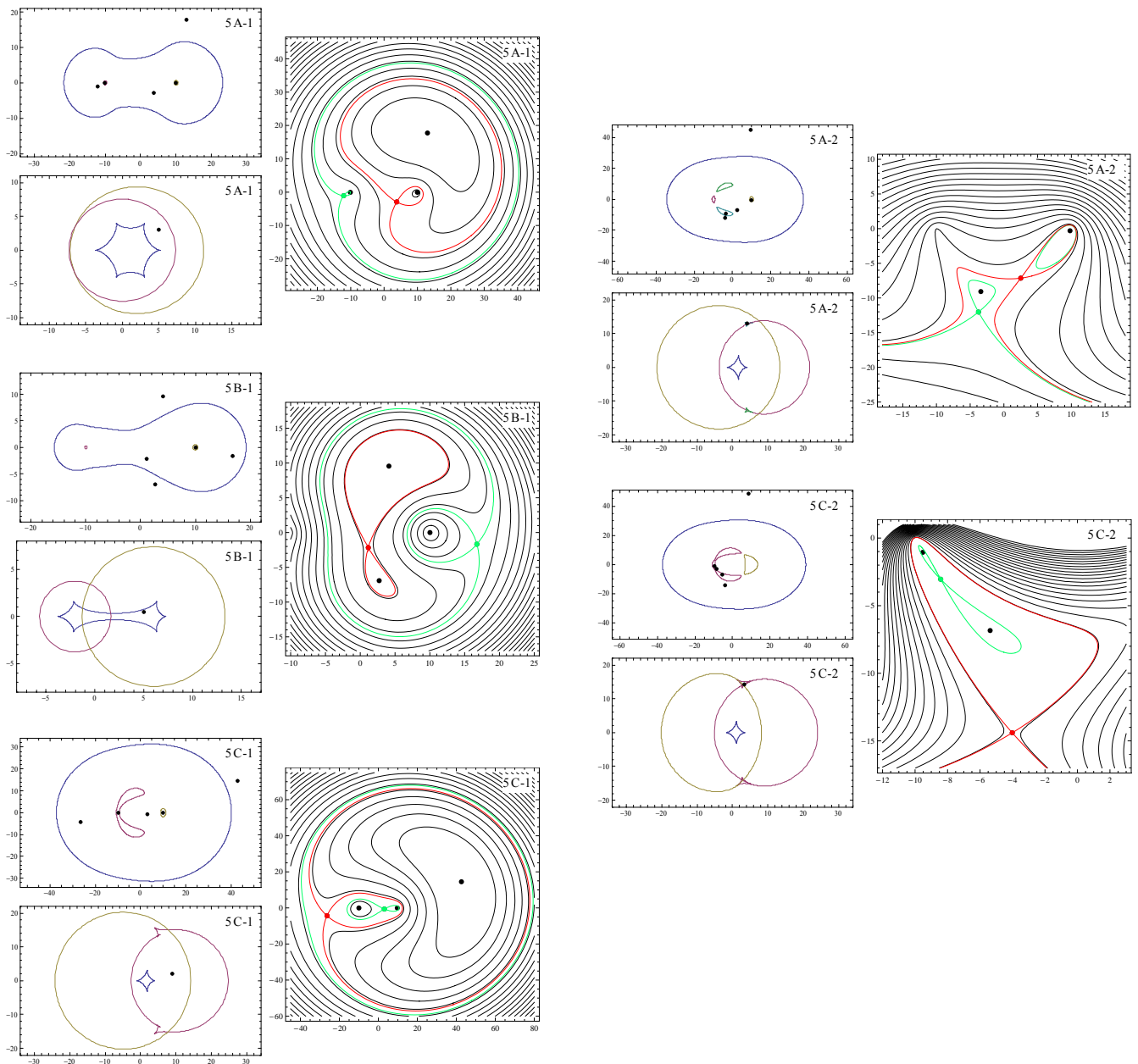


Figure 11. The different five-image Fermat surface topographies and image configurations (left- and right-hand panels as for Fig. 10). The saddle-point images coloured red arrive before those coloured green. Examples 5A-1 and 5C-1 would be observed as triplets because of the two highly-demagnified images near the galaxy centres at $(\pm 10, 0)$, whilst the others would be observed as quadruplets. 5A-2 and 5C-2 are qualitatively different image configurations that have the same critical isochrone topologies as 5A-1 and 5C-1, respectively. In 5A-2, the source is placed inside a three-cusp caustic and one of the radial critical curves, so only one of the five images is a highly demagnified core image. In 5C-2, a different choice of r_{c_1} and r_{c_2} is made so that a swallowtail cusp in the caustic that corresponds to the ‘Pacman’ critical curve can pierce the radial caustic. A source placed inside the swallowtail but outside the radial caustic gives five images, of which only one is highly demagnified.

the elliptic umbilic catastrophe in Type 2 critical curves (§ 4.4), and for the singular limit of Metamorphoses 3a and 3b (§ 4.5).

4.1 Pseudocaustics

The critical curves and caustics can still be of Type 0, 1 and 2 (with a mild abuse of terminology). The difference between the singular and cored cases is that the radial critical curves around the two galaxy centres shrink to zero size as the core radii decrease to zero. This means that there are no radial caustics, and that any core images move towards the centres of the isothermal spheres as $r_{c_1}, r_{c_2} \rightarrow 0$, their magnifications diminishing, until they disappear at the singularities. A source can therefore produce either an odd or an even number of images, depending on the number of

core images it would produce if the core radii were not zero. The number of images changes by one (with an image being created or destroyed at the centre of a singular isothermal sphere) when the source crosses a *pseudocaustic* (see e.g. Evans & Wilkinson 1998), a closed curve in the source plane which is approached by the radial caustics as $r_{c_1}, r_{c_2} \rightarrow 0$.

The positions of the pseudocaustics are easily found by considering the lens mapping on small circles around the singularities. In vector form, the lens equation reads

$$\xi = \mathbf{x} - E_1 \frac{\mathbf{x} + \mathbf{a}}{|\mathbf{x} + \mathbf{a}|} - E_2 \frac{\mathbf{x} - \mathbf{a}}{|\mathbf{x} - \mathbf{a}|}, \quad (10)$$

where $\mathbf{a} = (a, 0)$. Consider a small circle, say of radius δ , in the lens plane centred at the second singular isothermal sphere at \mathbf{a} . Then, as $\delta \rightarrow 0$, then $\mathbf{x} \rightarrow \mathbf{a}$ and $(\mathbf{x} + \mathbf{a}) \rightarrow (2\mathbf{a}, 0)$, whilst $E_2 (\mathbf{x} -$

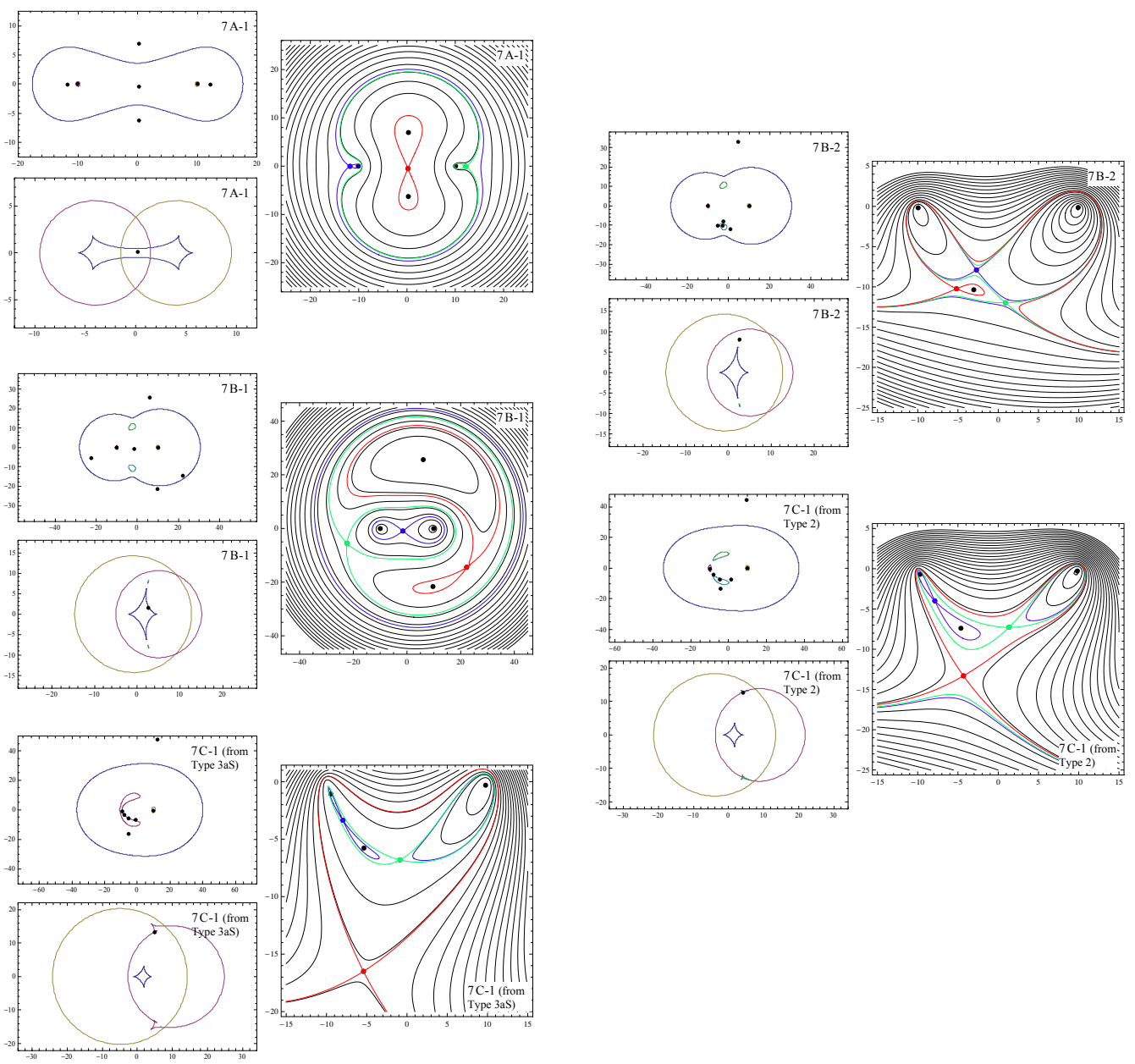


Figure 12. The different seven-image Fermat surface topographies and image configurations. The order of arrival of saddle-point images is red, green, blue. The two 7C-1 systems are not qualitatively different (although the image near $(-10, 0)$ is more demagnified), but arise from a topologically distinct caustic configurations. Except for the 7C-1 from Type 3aS caustics, and possibly the 7C-1 from Type 2 caustics, these would all be observed as quintuplets, as they each have two core images. 7B-2 has the same critical isochrone topology as 7B-1, but the image positions are very different and one of its critical isochrones (coloured red) is topologically a lemniscate but extremely distorted.

$a)/|\mathbf{x} - \mathbf{a}|$ becomes E_2 times a unit direction vector. So, the circle around the singularity at \mathbf{a} maps to a circle in the source plane centred at $(a - E_1, 0)$ and with radius E_2 . The other pseudocaustic, corresponding to the singularity at $-\mathbf{a}$ is found in the same way to be circle of radius E_1 , centred at $(-a + E_2, 0)$.

Figure 13 shows the critical curve and caustic configuration for a pair of singular isothermal spheres that, if cores were put in, would have been of Type 2 and near Metamorphosis 3a. The number of images produced by point sources in different regions is shown on the plot of the caustics. Since the radial critical curves have shrunk to points, Type 3a and 3b critical curves do not arise in the case of singular isothermal spheres. Instead, there remain two three-cusp caustics corresponding to the two small ‘bean’ critical curves of the Type 2 configuration, although these caustics become indefinitely elongated along one (both) pseudocaustics for $E_2 \geq 2a$ (respectively, $E_1 \geq 2a$), as the ‘bean’ critical curves then touch the singularities at $(\pm a, 0)$ (see § 4.5).

4.2 The Onset of Three- and Five-Fold imaging

When the singular isothermal spheres are far apart, so that their caustics and pseudocaustics do not overlap or join, then a point source can produce 1, 2 or 4 images. Each isothermal sphere has a circular pseudocaustic and a small astroid caustic within it, the size of which shrinks to zero as $a \rightarrow \infty$. A source outside the pseudocaustics produces 1 image, a source inside one of the pseudocaustics produces 2, and a source inside the astroid produces 4.

As a is decreased, triple imaging becomes possible when the pseudocaustics overlap. The condition on the lens parameters for overlapping pseudocaustics follows from their positions. It is

$$E_1 + E_2 > a. \quad (11)$$

Five-fold imaging becomes possible once part of an astroid caustic lies inside both pseudocaustics. The pseudocaustics are given in § 4.1, and it is straightforward to find the x -intercepts of

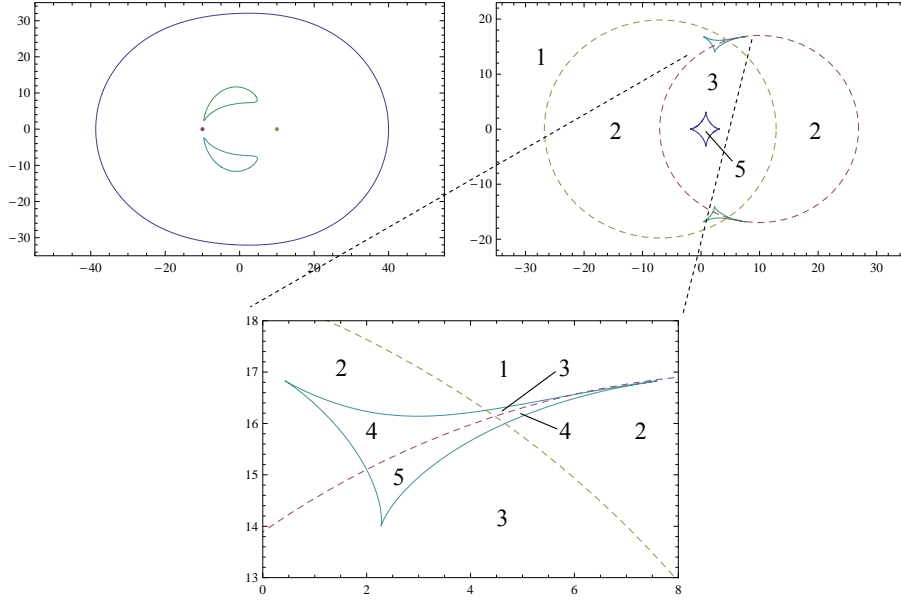


Figure 13. The left panel shows critical curves, and the right panel caustics (solid lines), for two singular isothermal spheres at $(-10, 0)$ and $(+10, 0)$ (marked by magenta and ochre dots). The pseudocaustics are the dotted circles; when a source crosses a pseudocaustic, a single image is created or destroyed at the corresponding singularity. The number of images for sources in different regions of the source plane are shown. If r_{c1} were raised from zero, the magenta pseudocaustic would become a true caustic as a small radial critical curve formed around $(-10, 0)$, and if r_{c1} were increased further, the three-cusp caustics would join with the magenta caustic as a ‘Pacman’ critical curve formed (Metamorphosis 3a). Raising r_{c2} from zero would make the ochre pseudocaustic a true caustic.

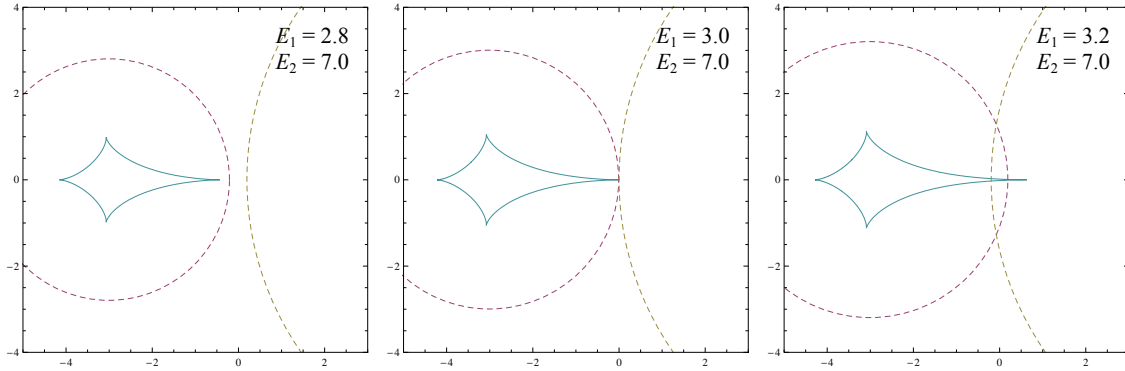


Figure 14. Close-up of the piercing of a pseudocaustic by an astroid caustic at the onset of five-fold imaging by a double-SIS lens. E_i increase from left to right panels. The astroid caustics are within their respective pseudocaustics unless the pseudocaustics overlap, when the astroid of the less-massive SIS (taken w.l.o.g. to be the left-hand one) pierces the pseudocaustic of that SIS, and therefore also overlaps with the region enclosed by both pseudocaustics.

the tangential critical curve(s), and hence the ξ -intercepts of the astroid caustic(s). This allows us to find the conditions on the lens parameters for which the pseudocaustics overlap with the astroid. Such overlapping is possible not only for Type 1 and 2 caustics, but also for Type 0. It turns out that, as a is decreased (or E_i increased), five-fold imaging becomes possible exactly when triple imaging does: when critical curves are of Type 0, the astroid of the second isothermal sphere stays wholly within its pseudocaustic (note we still take $E_1 < E_2$, without loss of generality), whilst the astroid of the first isothermal sphere pierces its pseudocaustic if and only if the pseudocaustics overlap (see Fig. 14). We now show this.

The critical curve of the first isothermal sphere cuts the x -axis at two points, and it is the right-hand one – call it x_{t1} – that maps to the right-hand cusp of the astroid that pierces the pseudocaustic

as shown in Fig. 14. From equations (2) and (7), the Jacobian along the x -axis for $r_{c1} = r_{c2} = 0$ is simple:

$$\det \mathbf{A}(x, 0) = 1 - \frac{E_1}{|x+a|} - \frac{E_2}{|x-a|}. \quad (12)$$

Now, x_{t1} lies between $-a$ and a , and the appropriate root of the quadratic (12) is

$$x_{t1} = \frac{1}{2} \left(E_1 - E_2 - \sqrt{B^2 - 4C} \right), \quad (13)$$

where $B = E_2 - E_1$ and $C = a(E_1 - E_2) - a^2$. The lens equation gives

$$\xi_{t1} = x_{t1} - E_1 + E_2. \quad (14)$$

Call the right-hand ξ -intercept of the first pseudocaustic ξ_{ps1} . We know from § 4.1 that

$$\xi_{ps1} = -a + E_2 + E_1. \quad (15)$$

Now, the astroid pierces the pseudocaustic if and only if $\xi_{t1} > \xi_{ps1}$, that is, combining the three equations above, if

$$2a - 3E_1 - E_2 - \sqrt{(E_2 - E_1)^2 + 4a(a - E_1 - E_2)} > 0, \quad (16)$$

which, on squaring and cancelling terms, is equivalent to

$$(a - 2E_1)(a - E_1 - E_2) > a(a - E_1 - E_2). \quad (17)$$

We are considering critical curves of Type 0, and so – anticipating the result (23) from the next section together with the assumption $E_1 \leq E_2$ – (17) reduces to

$$a - E_1 - E_2 < 0, \quad (18)$$

which is exactly the condition (11) for overlapping pseudocaustics. (A similar calculation shows that the astroid caustic of the second isothermal sphere does not pierce the second pseudocaustic.)

Calculations for the left- and right-most astroid cusps on the ξ -axis, corresponding to critical points at $x < -a$ and $x > a$, show that five-fold imaging is always possible if the critical curves and caustics are of Type 1 or Type 2 (with $E_1 \leq E_2 \leq 2a$). However, the astroid may lie entirely outside the first pseudocaustic if $E_2 > 2a$. In this case, there is still overlapping if

$$E_2(E_2 - E_1) < a(2E_2 - E_1). \quad (19)$$

4.3 The First Metamorphosis

By (4) and direct differentiation of the deflection potential (1), the Jacobian of the lens mapping for two isothermal spheres reduces, along the x -axis, to

$$\det \mathbf{A}(x, 0) = R(x)T(x), \quad (20)$$

where roots of

$$R(x) \doteq 1 - \frac{E_1 r_{c1}^2}{[r_{c1}^2 + (x+a)^2]^{3/2}} - \frac{E_2 r_{c2}^2}{[r_{c2}^2 + (x-a)^2]^{3/2}}, \quad (21a)$$

$$T(x) \doteq 1 - \frac{E_1}{[r_{c1}^2 + (x+a)^2]^{1/2}} - \frac{E_2}{[r_{c2}^2 + (x-a)^2]^{1/2}}, \quad (21b)$$

give radial and tangential critical points, respectively. If $T(x) = 0$ has two roots for $x \in (-a, a)$, then the critical curves are of Type 0 (there are two separate tangential critical curves). For singular isothermal spheres, $R(x) \equiv 1$. There are no radial critical curves, and the three equations above reduce to (12), that is,

$$\det \mathbf{A}(x, 0) = T(x) = 1 - \frac{E_1}{|x+a|} - \frac{E_2}{|x-a|}.$$

For $x \in (-a, a)$, $T(x)$ is concave down with a single maximum at some x_m . $T'(x) = 0$ is a quadratic in x with one root in this interval, and we find

$$x_m = -a \frac{\sqrt{E_2} - \sqrt{E_1}}{\sqrt{E_2} + \sqrt{E_1}}. \quad (22)$$

If $T(x_m) > 0$, there are two roots; if $T(x_m) < 0$, there are no roots. If $T(x_m) = 0$, the tangential critical curves are touching and this is Metamorphosis 1. Combining the two previous equations, $T(x_m)$ reads

$$\frac{1}{2a} \left(\sqrt{E_1} + \sqrt{E_2} \right)^2 = 1. \quad (23)$$

Critical curves are of Type 0 if the left-hand side (LHS) is less than 1 and Type 1 if LHS > 1 . It is clear that (23) remains a

very good approximation for the non-singular isothermal spheres if $r_{c1}, r_{c2} \ll a$.

4.4 The Elliptic Umbilic Catastrophe

The radial and tangential critical curves are well-known from single spherical or elliptical lenses. In such cases, the Jacobian of the lens mapping, $\det \mathbf{A}$, is positive immediately around the galaxy centre, negative between the radial and tangential critical curves, and positive outside the tangential critical curve, where $\det \mathbf{A} \rightarrow 1$ as $|\mathbf{x}| \rightarrow \infty$. We intuitively expect a double isothermal sphere lens to have Type 0 critical curves when the separation $2a$ is large, and for the tangential critical curves to merge to give Type 1 when the isothermal spheres are brought closer together. The possibility of Type 2 critical curves, with ‘bean’ critical curves, may not be as intuitively obvious.

The ‘bean’ critical curves surround small regions of positive $\det \mathbf{A}$ inside the common tangential critical curve, where $\det \mathbf{A}$ is otherwise negative. The physical reason that these regions must exist is that there are points where the shear is zero (c.f. discussion of the two point-mass lens in Schneider et al. (1992) §8.3). From the expression (5) for $\det \mathbf{A}$, if $\gamma(\mathbf{x}) = 0$ at some \mathbf{x} , then $\det \mathbf{A}(\mathbf{x}) > 0$.

For the double isothermal sphere lens, there are indeed two points where $\gamma = 0$ because the shears from the two isothermal spheres cancel out. Let us begin by showing that, if the isothermal spheres (singular or not) are located at $(\pm a, 0)$, the points of zero shear lie on a circle of radius a centred at the origin. It is useful to define the angle of shear ω in the usual manner and write the shear as the complex (polar) quantity

$$\Gamma \doteq \gamma_1 + i\gamma_2 \equiv \gamma e^{2i\omega}. \quad (24)$$

(Note that $\omega \mapsto \omega \pm \pi$ has no physical effect.) Now, since the deflection potential of two isothermal spheres is the sum of their two separate deflection potentials, the (complex) shear is also the sum of two separate shears: $\Gamma = \Gamma^{(1)} + \Gamma^{(2)}$. Therefore, if the shear is zero at some point \mathbf{x} , we must have

$$\omega^{(2)}(\mathbf{x}) = \omega^{(1)}(\mathbf{x}) + \frac{(2k+1)\pi}{2} \quad k \in \mathbb{Z}. \quad (25)$$

For an isothermal sphere, the direction of shear $\omega^{(j)}(\mathbf{x})$ at a point \mathbf{x} must, by symmetry, be either

$$\omega^{(j)}(\mathbf{x}) = \theta_j \quad \text{or} \quad \omega(\mathbf{x}) = \theta_j - \frac{\pi}{2}, \quad (26)$$

where θ_j is the direction of \mathbf{x} from the centre of the j th isothermal sphere. (It turns out to be the latter.) Therefore, (25) holds if

$$\theta_2 - \theta_1 = \pm \frac{\pi}{2}, \quad (27)$$

that is, if the line segment joining $(-a, 0)$ to \mathbf{x} is perpendicular to that joining $(a, 0)$ to \mathbf{x} . The locus of such points \mathbf{x} is the circle with the two galaxy centres as its diameter, $|\mathbf{r}| = a$ (see Fig. 15).

It remains to show that there must exist two points on this circle for which $\gamma^{(1)} = \gamma^{(2)}$. For a single isothermal sphere, the magnitude of shear is

$$\gamma^{(j)} = \frac{1}{2} E_j \frac{r_j^2}{(r_c^2 + r_j^2)^{(3/2)}}, \quad (28)$$

where r_j is the distance from its centre. As we are only considering $r_{c1}, r_{c2} \ll a, E_1, E_2$, at points on the circle close enough to the first isothermal sphere (the one at $(-a, 0)$), we have $\gamma^{(1)} > \gamma^{(2)}$, whilst the reverse inequality holds at points close enough to

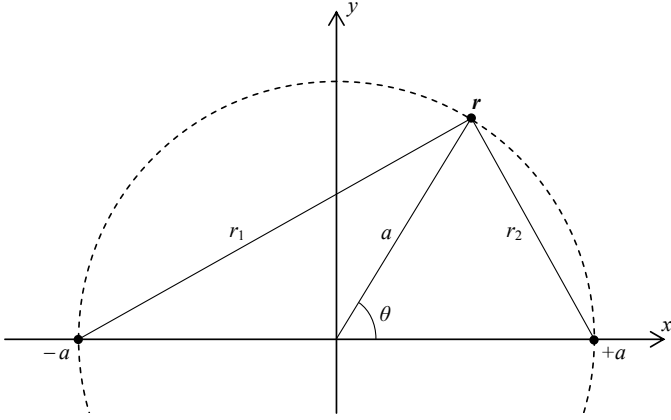


Figure 15. The point of zero shear lies on the circle $|\mathbf{r}| = a$. The centres of the (singular or cored) isothermal spheres are at $\pm a$ on the x -axis.

the second isothermal sphere. There are therefore two points in-between (one in the $y > 0$ semicircle and the other in the $y < 0$) where equality holds.

Although this result does not allow the conditions for Metamorphosis 2 to be determined analytically, it does allow us to find the lens parameters at which the elliptic umbilic catastrophe occurs: it occurs when the point of zero shear is also a critical point. We first need to know the (polar) coordinates (a, θ_{zs}) of the point of zero shear. Recalling that r_1 and r_2 are the distances between a point \mathbf{r} and the centres of the isothermal spheres, on the circle $|\mathbf{r}| = a$ we have

$$r_1^2 = 2a^2(1 + \cos \theta), \quad r_2^2 = 2a^2(1 - \cos \theta) \quad (29)$$

by the cosine rule (see Fig. 15). Now, by (28), the point of zero shear for the double lens has

$$\frac{r_1}{r_2} = \frac{E_1}{E_2}, \quad (30)$$

and combining this with (29) yields the result

$$\cos \theta_{zs} = \frac{E_1^2 - E_2^2}{E_1^2 + E_2^2}. \quad (31)$$

An elliptic umbilic catastrophe occurs at the point of zero shear (where the surrounding critical curves – and the corresponding three-cusp caustics – shrink to zero size) when

$$a = \frac{1}{2} \sqrt{E_1^2 + E_2^2}. \quad (32)$$

This is proved as follows. From (5), at the point of zero shear,

$$\det \mathbf{A} = (1 - \kappa)^2 \quad (33)$$

where the convergence κ is

$$\kappa(r, \theta) = \kappa^{(1)} + \kappa^{(2)} = \frac{E_1}{2r_1} + \frac{E_2}{2r_2}. \quad (34)$$

Now, r_1 and r_2 at the point of zero shear are given in terms of E_1, E_2 and a by (29) and (31), and putting (34) into $(1 - \kappa)^2 = 0$ yields, after some algebra, (32).

4.5 The Singular Limit of Metamorphoses 3a and b

As $E_2 \rightarrow 2a$ or $E_1 \rightarrow 2a$ from below, the ‘bean’ critical curves (that surround points of zero shear) approach the singularity at $(-a, 0)$ or $(a, 0)$, respectively, as illustrated in Fig. 16. This can

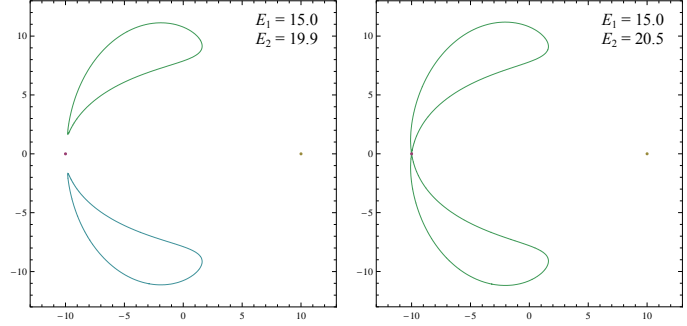


Figure 16. The inner critical curves of two singular isothermal spheres for $a = 10$. The ‘bean’ critical curves meet at the singularity when E_2 reaches $2a = 20$.

be seen from two observations.

First, near the singularities at $(\pm a, 0)$, $\det \mathbf{A} < 0$ on the x -axis by inspection of (12). Secondly, along the circle $|\mathbf{r}| = a$, $\det \mathbf{A} < 0$ near $(a, 0)$ or $(-a, 0)$ if and only if $E_1 < 2a$ or $E_2 < 2a$, respectively. This follows from inspection of

$$\det \mathbf{A}(a, \theta) = \frac{1}{2a^2 \sin \theta} \left[E_1 E_2 + 2a^2 |\sin \theta| - 2a (E_1 |\sin(\theta/2)| + E_2 |\cos(\theta/2)|) \right], \quad (35)$$

which can be obtained – a little tediously but straightforwardly – either from

$$\det \mathbf{A}(r, \theta) = \frac{1}{r} \begin{vmatrix} \partial \xi / \partial r & \partial \xi / \partial \theta \\ \partial \eta / \partial r & \partial \eta / \partial \theta \end{vmatrix} \quad (36)$$

(with the derivatives being evaluated directly from the lens equation in polar coordinates), or from (5), (29), (34) and

$$\gamma(a, \theta) = |\gamma^{(1)} - \gamma^{(2)}| = \frac{1}{2} \left| \frac{E_1}{r_1} - \frac{E_2}{r_2} \right|. \quad (37)$$

5 EXTERNAL SHEAR OR INTERNAL ELLIPTICITY

In this section, we investigate two astrophysically important effects. First, Binary galaxies may be embedded in a loose group or cluster (as in fact is the case for CASSOWARY 2), in which case tidal shear will distort the caustics and critical curves. Second, galaxies are characteristically flattened, and so internal ellipticity will also play a role. In this section, we introduce simple models in § 5.1, survey the principal effects in § 5.2 and give some analytic results in § 5.3

5.1 Models

5.1.1 External Shear

The effects of a larger-scale gravitational field, arising from the environment in which the lens sits, are often approximated by external shear: the quadratic terms of the large-scale field expanded about the centre of the lens. With suitable translation of the source-plane coordinates, the lens equation including external shear is

$$\begin{pmatrix} \xi \\ \eta \end{pmatrix} = \begin{pmatrix} x \\ y \end{pmatrix} - \begin{pmatrix} \psi_x(x, y) \\ \psi_y(x, y) \end{pmatrix} - P \begin{pmatrix} x \\ y \end{pmatrix} \quad (38)$$

where ψ is the deflection potential of the two isothermal spheres and

$$P = \begin{pmatrix} \gamma \cos 2\phi & \gamma \sin 2\phi \\ \gamma \sin 2\phi & -\gamma \cos 2\phi \end{pmatrix} \quad (39)$$

is the external shear matrix, and γ and ϕ are the magnitude and angle of external shear respectively. (Note that $\phi = 0$ corresponds to shear from a perturbing mass at ∞ or $-\infty$ on the y -axis). The Jacobian of the lens mapping becomes

$$\det \mathbf{A} = (1 - \psi_{xx} - P_{11})(1 - \psi_{yy} - P_{22}) - (\psi_{xy} + P_{12})^2. \quad (40)$$

By the arguments of § 4, the pseudocaustics are still circles of radii E_1 and E_2 , but are now centred at

$$(-a + E_2 + \gamma a \cos 2\phi, \gamma a \sin 2\phi) \quad (41a)$$

and

$$(a - E_1 - \gamma a \cos 2\phi, -\gamma a \sin 2\phi). \quad (41b)$$

5.1.2 Ellipticity

Galaxies are also characteristically flattened. One commonly used flattened generalization of the isothermal sphere is the pseudo-isothermal elliptic potential (see e.g. Kassiola & Kovner 1993; Hunter & Evans 2001; Evans & Hunter 2002), which coincides with the isothermal sphere model when its ellipticity parameter ϵ is zero, and otherwise has elliptical isopotentials with axis ratio $(1 + \epsilon)/(1 - \epsilon)$. The models are the projections of the power-law galaxies studied by Evans (1994). When the isothermal spheres at $(\pm a, 0)$ are replaced with this model, the deflection potential of the lens becomes

$$\psi(x, y) = \frac{E_1}{(r_{c,1}^2 + r_1^2)^{1/2}} + \frac{E_2}{(r_{c,2}^2 + r_2^2)^{1/2}} \quad (42)$$

where

$$\begin{aligned} r_1^2 &= x'^2(1 - \epsilon) + y'^2(1 + \epsilon) \\ r_2^2 &= x''^2(1 - \epsilon) + y''^2(1 + \epsilon) \end{aligned} \quad (43)$$

and (x', y') and (x'', y'') are Cartesians centred on $(-a, 0)$ and $(a, 0)$ inclined at ϕ_1 and ϕ_2 to the x -axis respectively.

5.2 Effects on Critical Curves, Caustics and Image Multiplicity

A numerical investigation of the critical curves and caustics illustrates the essential differences between these models and the two isothermal spheres. For realistic values of shear or ellipticity, no dramatically different critical curve topologies arise, although there are minor differences resulting from the breaking of the reflection symmetry about the x -axis: Metamorphoses 2, 3a, and 3b can occur in two steps, with one ‘bean’ critical curve being created, or merging with a radial critical curve, before the other one – examples are presented in the panels of Figs. 17 and 18.

More interestingly perhaps, the maximum number of images can change with the addition of shear or ellipticity. Of course, when shear or ellipticity is added to a single, isolated isothermal sphere, the maximum possible number of images increases from three to five (or from two to four in the singular case) because the tangential caustic, which had been a single point, becomes an astroid caustic with the breaking of circular symmetry. There is not always such a dramatic difference when shear or ellipticity is added to a double isothermal sphere lens, because circular symmetry has already been broken. However, the tangential critical curve(s) is (are) distorted by shear (see, for example, the left panel of Fig. 21). Shear

with $\phi \approx 0^\circ$, or ellipticity with $\phi_i \approx 90^\circ$, can lead to extra cusps forming in the tangential caustic(s), which can then self-overlap. When there are two separate tangential caustics, this can increase the maximum number of images from five to seven (from four to six in the singular case); when there is a common tangential caustic, there can be regions of nine- and even eleven-fold imaging (seven- or nine-fold for the singular case).

The left panel of Fig. 19 shows the caustics for two cored isothermal spheres in moderately strong external shear aligned close to the x -axis. The originally six-cusped caustic develops four extra cusps, and the self-overlapping creates regions of high-order imaging: Source 1 is imaged nine times, and Source 2 imaged eleven times. The right-hand panels of Fig. 19 show the Fermat surfaces for the two sources, along with image positions and the critical isochrones. Note that the elevenfold imaging configuration bears a remarkable similarity to the recently discovered lens CAS-SOWARY 2, although of course this is not a fit.

5.3 Analytic Results

One simple result remains analytic for a double isothermal sphere lens in external shear: the touching of the two critical curves along the x -axis. When the isothermal spheres are far apart, the shear distorts the tangential caustics into ellipses with minor axes aligned with the direction of external shear, as expected from the effect of shear on one isothermal sphere (see e.g. Schneider et al. 2006). The tangential caustics are of course no longer ellipses when the isothermal spheres are brought closer together, but they still tend to be stretched in the direction perpendicular to the external shear. We expect shear with $\phi = 0^\circ$ (90°) to shift Metamorphosis 1 to larger (smaller) E_1, E_2 compared to the shearless case. This is indeed the case.

There is a complication, however. Since even a small nonzero γ at $\phi \neq 0^\circ, 90^\circ$ distorts the critical curves (see Figs. 20 and 21) and destroys the reflection symmetry in the x -axis, it is no longer clear that $\det \mathbf{A}(x, y)$ must have a saddle point on the x -axis as it did when there was no external shear. Indeed, the two tangential critical curves do not necessarily first merge at the x -axis: for very strong shear ($\gamma \gtrsim 0.45$ for $a = 10$) and small ϕ , the tangential critical curves may merge at two points above and below the x -axis first, giving rise to new critical curve geometries, examples of which are shown in the panels of Fig. 20. These new critical curve metamorphoses don’t occur if there is internal ellipticity but no shear.

However, as we now show, in the case of singular isothermal spheres, there is still always a saddle point in $\det \mathbf{A}(x, y)$ on the x -axis, which, for reasonable values of γ , is the point at which the tangential critical curves first touch (when $\det \mathbf{A} = 0$ at the saddle point). First, we obtain $\nabla \det \mathbf{A}$ from (40) and direct differentiation. Restricted to the x -axis, we have

$$\frac{\partial}{\partial x} \det \mathbf{A} = \left(\frac{E_1(x+a)}{|x+a|^3} + \frac{E_2(x-a)}{|x-a|^3} \right) (1 - \gamma \cos 2\phi), \quad (44a)$$

$$\frac{\partial}{\partial y} \det \mathbf{A} = \left(\frac{E_1(x+a)}{|x+a|^3} + \frac{E_2(x-a)}{|x-a|^3} \right) 2\gamma \sin 2\phi, \quad (44b)$$

so it is clear that there is one stationary point on the x -axis for $x \in (-a, a)$ because $\frac{\partial}{\partial x} \det \mathbf{A}|_{y=0}$ and $\frac{\partial}{\partial y} \det \mathbf{A}|_{y=0}$ have a common root. This stationary point is a maximum of

$$\det \mathbf{A}(x, 0) = \left(1 + \gamma \cos 2\phi - \frac{E_1}{|x+a|} - \frac{E_2}{|x-a|} \right)$$

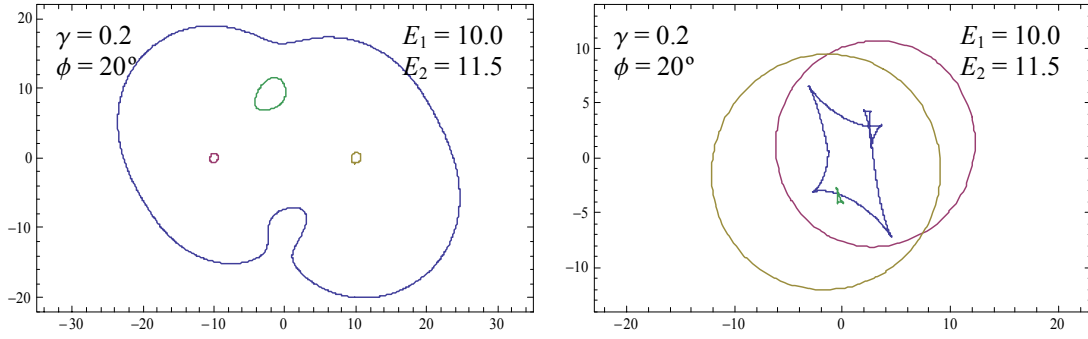


Figure 17. The critical curves (left panel) and caustics (right panel) of two isothermal spheres in moderately strong external shear. With shear not along the x or y axes, Metamorphosis 2, the splitting-off of two ‘bean’ critical curves from the common tangential critical curve, is split into two separate metamorphoses as one ‘bean’ is created before the other.

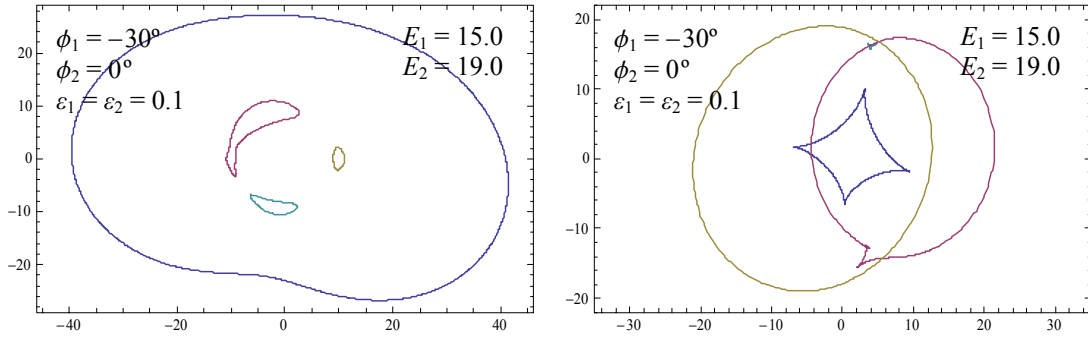


Figure 18. The critical curves (left panel) and caustics (right panel) of two pseudo-isothermal elliptical potentials both with $\epsilon = 0.1$. Unless the axes of the elliptical potentials are both aligned with the x or y axes, Metamorphosis 3a is split into two separate metamorphoses as one ‘bean’ critical curve merges with a radial critical curve before the other does. Metamorphosis 3b is similarly split.

$$\times (1 - \gamma \cos 2\phi) - \gamma^2 \sin^2 2\phi, \quad (45)$$

which for $\gamma = 0$ reduces to (12). By the argument of § 4.3, the tangential critical curves touch each other on the x -axis when

$$(1 - \gamma \cos 2\phi) \left(1 + \gamma \cos 2\phi - \frac{(\sqrt{E_1} + \sqrt{E_2})^2}{2a} \right) = \gamma^2 \sin^2 2\phi. \quad (46)$$

The condition on the lens parameters for this metamorphosis is the analogue in the unsheared case of (23). There is always a saddle on the x -axis, no matter how large γ is. However, the merger that occurs at the saddle on the x -axis may not be the first such merger between the two tangential critical curves if γ is large, as illustrated in the panels of Fig. 20. Eqn (46) gives the condition for the bottom-left panel changing to the bottom-right. Once again, this criterion holds approximately if r_{c_1}, r_{c_2} are small but nonzero.

6 CONCLUSIONS

This paper has provided a detailed investigation into the lensing properties of binary galaxies, modelled as two isothermal spheres with different velocity dispersions. Such models are useful for describing strong lenses in which two close galaxies bend light rays emanating from a more distant source. With the addition of external shear, the models can also represent groups or clusters dominated by a pair of massive galaxies. This is of course a very common

circumstance, with about a quarter of all strong lenses showing evidence for lensing by pairs or groups of galaxies.

Our paper extends and generalizes the previous binary lens work of Schneider & Weiss (1986), who used two point masses. Binary isothermal spheres differ qualitatively from the better-known case of two point masses by having additional critical curves and caustics (or pseudocaustics in the case of singular isothermal spheres), and therefore also different multiple-imaging properties. If the isothermal spheres have cores, then the number of images can be 1, 3, 5 or 7, depending on the location of the source, the separation of the binary and the velocity dispersions. If the isothermal spheres are coreless, then the number of images may be 1, 2, 3, 4 or 5. This lens model is sufficiently simple that many of the properties can be derived analytically, or nearly so. We have described the shapes of the caustics and critical curves for the case of equal and unequal masses, have studied the principal metamorphoses and have classified the critical isochrone topologies. Finally, we presented a brief survey of the effects of the inclusion of external shear and internal flattening.

For comparison with the real world, it is helpful for us to show how our models relate to physical systems. The typical velocity dispersion of a large elliptical galaxy is $\sigma \sim 250\text{-}300 \text{ km s}^{-1}$, while typical core radii are in the range $\sim 10\text{-}100 \text{ pc}$. Given a typical lens redshift of $z_1 \sim 0.5$ and source redshift of $z_s \sim 2$, then the corresponding Einstein radius of an isolated isothermal sphere is $\sim 10 \text{ kpc}$. The effects studied in this paper become important if two galaxies are separated by $\lesssim 4$ Einstein radii (see e.g., Fig 1). At the typical redshifts, this corresponds to a separation of $\lesssim 40$

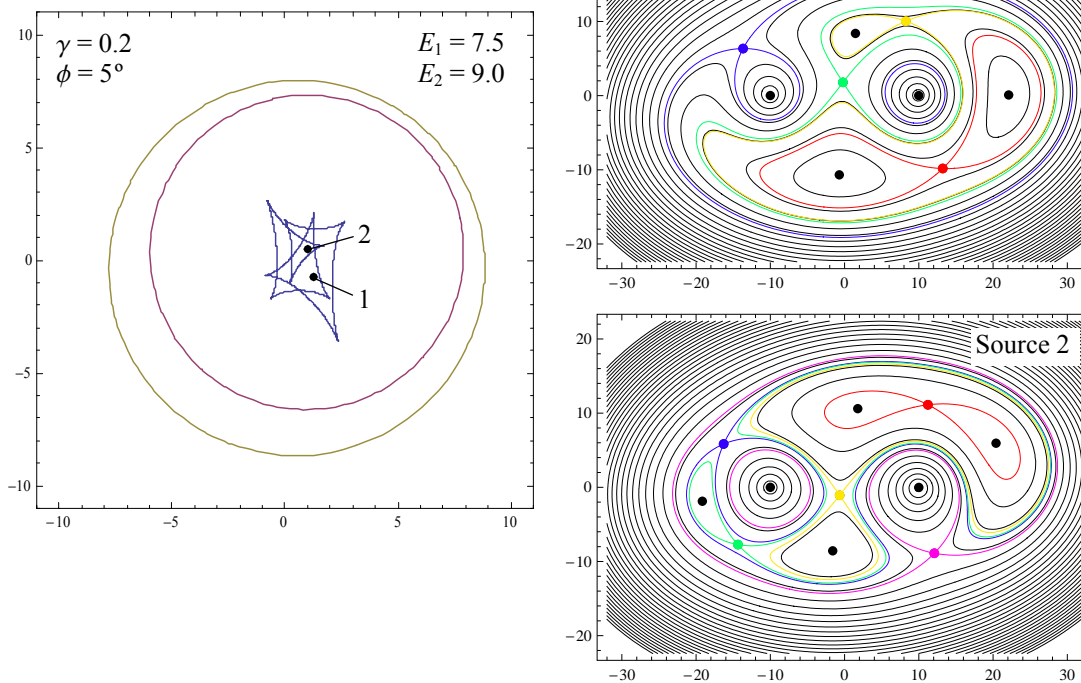


Figure 19. The lens here is two cored isothermal spheres at $(\pm a, 0)$ with external shear of $\gamma = 0.2$ in the direction $\phi = 5^\circ$. Without shear the critical curves and caustics would be Type 1. The positions of two point sources are shown with the caustics in the left panel; the right panels are contours of the Fermat potential for the two sources, together with saddle-point images and their critical isochrones (coloured points and lines) and the images (black points) corresponding to Fermat maxima and minima. The order of arrival of the saddle-point images is red, yellow, green, blue, magenta. The four saddles of the nine-image case give a critical isochrone topology $\text{Li}^+ \text{Li}^+ \text{Le}^- \text{Le}^-$, and two of the images are probably unobservable ‘core’ images; the five saddles of eleven-image case give $\text{Li}^+ \text{Li}^+ \text{Le}^- \text{Le}^- \text{Le}^-$ and nine of the images are observable.

kpc (or $\lesssim 5''$). A good example is provided by CASSOWARY 5, which has two lensing galaxies separated by $\sim 5''$ (Belokurov et al. 2008). The three images straddle the two lensing galaxies, much as the illustration in the lower panel of Fig. 10. CASSOWARY 5 looks like an example of our image configuration 3B-1, though it important to bear in mind that the existing, primarily Sloan Digital Sky Survey, data is comparatively shallow ($r \lesssim 23$). Deeper follow-up imaging may reveal the presence of more images in CASSOWARY 5.

There are some interesting ways to extend the work in this paper. First, the effects of nearby galaxies are often modelled with external shear, so a thorough comparison of the properties of binary isothermal lenses with the single isothermal lens plus shear is warranted. As is well-known, the Chang-Refsdal lens (or point mass plus external shear) is only partially successful in describing the lensing properties of binary point masses. Second, although we have sketched the principal effects of flattening and shear here, it would be interesting to prove the maximum number of possible images. The fact that caustics can have points of self-intersection means that regions of the source plane are created for which very high-order imaging is possible. Third, there are still very few highly non-axisymmetric lenses that have been studied. The binary lens (whether point masses or double galaxies) is one example, but it would be interesting to study the lensing properties of needles, filaments, and sheets, as well. These may have applications to highly prolate or highly flattened galaxies, which are the natural end-points of the Newtonian collapse of spheroids of collisionless matter (Lin et al. 1965).

ACKNOWLEDGEMENTS

EMS acknowledges financial support from the Commonwealth Scholarship Commission and Cambridge Commonwealth Trust. This research has been supported by the ‘ANGLES’ European Union Research and Training Network for gravitational lensing. We thank an anonymous referee for a careful reading of the manuscript.

REFERENCES

- An J. H., et al. 2002, *ApJ*, 572, 521
- An J. H., Evans N. W. 2006, *MNRAS*, 369, 317
- Arnold, V.I. 1986, *Catastrophe Theory*, Springer Verlag, New York
- Asada H. 2002, *A&A*, 390, L11
- Beaulieu J.-P., et al. 2006, *Nat*, 439, 437
- Belokurov V., et al. 2007, *ApJ*, 671, L9
- Belokurov V., et al. 2008, *ApJ*, submitted
- Blandford R., Narayan R. 1986, *ApJ*, 310, 568
- Bradač M., Schneider P., Lombardi M., Steinmetz M., Koopmans L. V. E., Navarro J. F. 2004, *A&A*, 423, 797
- Chang K., Refsdal S. 1984, *A&A*, 132, 168
- Evans N. W. 1994, *MNRAS*, 267, 333
- Evans N. W., Wilkinson M. I. 1998, *MNRAS*, 296, 800
- Evans N. W., Witt H. J. 2001, *MNRAS*, 327, 1260
- Evans N. W., Hunter C. 2002, *ApJ*, 575, 68

Micro, Springer-Verlag, Berlin
 Shin E.M., Evans N.W., 2008, MNRAS, MNRAS, 385, 2107
 Winn J.N., Kochanek C.S., Keeton C.R., Lovell J.E.J., 2003, ApJ, 590, 26
 Wisotzki L., Christlieb N., Liu M. C., Maza J., Morgan N. D., Schechter P. L. 1999, A&A, 348, L41
 Witt H. J. 1990, A&A, 236, 311
 Witt H. J., Mao S. 1995, ApJ, 447, L105

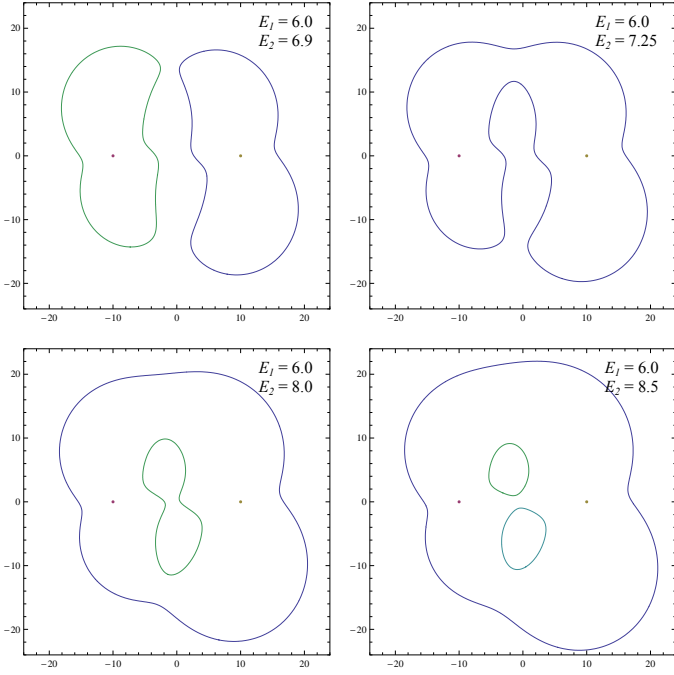


Figure 20. Critical curves of lenses with two singular isothermal spheres (dots at $(\pm a, 0)$) in very strong external shear. In all four panels, the external shear is $\gamma = 0.5$, $\phi = 10^\circ$. The strong shear distorts the tangential caustics of the singular isothermal spheres. In particular, it prevents them merging on the x -axis until E_i are much larger: without external shear, the lenses in all four panels would have a single common tangential caustic. The condition (46) holds at the transition between the topologies of the bottom-left and bottom-right panels.

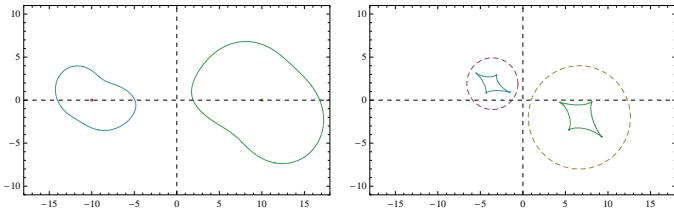


Figure 21. The critical curves (left panel) and caustics (right panel) of a double singular isothermal sphere lens with $a = 10$, $E_1 = 3.0$, $E_2 = 6.0$ and moderate external shear ($\gamma = 0.2$) in the direction $\phi = 40^\circ$, which distorts the tangential critical curves (and caustics). It is believable, but not obvious, that the critical curves will meet on the x -axis if E_i are increased.

Faure C., Alloin D., Kneib J. P., Courbin F. 2004, A&A, 428, 741
 Hunter C., Evans N.W., 2001, ApJ, 554, 1227
 Kassiola A., Kovner I., 1993, ApJ, 417, 450
 Keeton C. R., Mao S., Witt H. J. 2000, ApJ, 537, 697
 Kochanek C. S., & Apostolakis, J. 1988, MNRAS, 235, 1073
 Lin C. C., Mestel L., Shu F. H. 1965, ApJ, 142, 1431
 Mao S., Paczynski B. 1991, ApJ (Letters), 374, L37
 Petters A. O., Levine H., Wambsganss J., Singularity theory and gravitational lensing, Birkhäuser, 2001
 Rusin D., et al. 2001, ApJ, 557, 594
 Schneider P., Weiss A. 1986, A&A, 164, 237
 Schneider P., Ehlers J., Falco E.E., 1992, Gravitational Lenses, Springer-Verlag, New York
 Schneider P., Kochanek C.S., & Wambsganss J., 2006, Saas-Fee Advanced Course 33: Gravitational Lensing: Strong, Weak and